QUANTUM SENSORS PROGRAM

Harris Corporation

Sponsored by
Defense Advanced Research Projects Agency
DARPA Order No. AJ10/00

APPROVED FOR PUBLIC RELEASE; DISTRIBUTION UNLIMITED.

STINFO COPY

AIR FORCE RESEARCH LABORATORY
INFORMATION DIRECTORATE
ROME RESEARCH SITE
ROME, NEW YORK

NOTICE AND SIGNATURE PAGE

AFRL-RI-RS-TR-2009-208 HAS BEEN REVIEWED AND IS APPROVED FOR PUBLICATION IN ACCORDANCE WITH ASSIGNED DISTRIBUTION STATEMENT.

FOR THE DIRECTOR:

/s/   /s/
DONALD J. NICHOLSON   EDWARD J. JONES, Deputy Chief
Work Unit Manager   Advanced Computing Division
                                                        Information Directorate

REPORT DOCUMENTATION PAGE			*Form Approved* **OMB No. 0704-0188**

Public reporting burden for this collection of information is estimated to average 1 hour per response, including the time for reviewing instructions, searching data sources, gathering and maintaining the data needed, and completing and reviewing the collection of information. Send comments regarding this burden estimate or any other aspect of this collection of information, including suggestions for reducing this burden to Washington Headquarters Service, Directorate for Information Operations and Reports, 1215 Jefferson Davis Highway, Suite 1204, Arlington, VA 22202-4302, and to the Office of Management and Budget, Paperwork Reduction Project (0704-0188) Washington, DC 20503.
PLEASE DO NOT RETURN YOUR FORM TO THE ABOVE ADDRESS.

1. REPORT DATE *(DD-MM-YYYY)* AUGUST 2009	**2. REPORT TYPE** Final		**3. DATES COVERED** *(From - To)* August 2007 – June 2009
4. TITLE AND SUBTITLE QUANTUM SENSORS PROGRAM			**5a. CONTRACT NUMBER** FA8750-07-C-0206
			5b. GRANT NUMBER N/A
			5c. PROGRAM ELEMENT NUMBER 61101E
6. AUTHOR(S) G. Burdge, G. Deibner, J. Shaprio, F. Wong, P. Kumar, H. Yuen, M. Vasilyev, N. Stelmakh, Z. Dutton, S. Guha, and J. Habif			**5d. PROJECT NUMBER** AJ10
			5e. TASK NUMBER QU
			5f. WORK UNIT NUMBER SE
7. PERFORMING ORGANIZATION NAME(S) AND ADDRESS(ES) Harris Corporation P.O. Box 37, MS 13-11A Melbourne, FL 32902-0037			**8. PERFORMING ORGANIZATION REPORT NUMBER** N/A
9. SPONSORING/MONITORING AGENCY NAME(S) AND ADDRESS(ES) AFRL/RITC 525 Brooks Road Rome NY 13441-4505			**10. SPONSOR/MONITOR'S ACRONYM(S)** N/A
			11. SPONSORING/MONITORING AGENCY REPORT NUMBER AFRL-RI-RS-TR-2009-208

12. DISTRIBUTION AVAILABILITY STATEMENT
APPROVED FOR PUBLIC RELEASE; DISTRIBUTION UNLIMITED. PA# 88ABW-2009-3763 Date Cleared: 27-August-2009

13. SUPPLEMENTARY NOTES

14. ABSTRACT
The resolution of a homodyne LADAR can be enhanced significantly by applying quantum optical techniques in the receiver. With a quantum image enhancer (QIE) inserted between the receive optics and the detector of a LADAR, an angular cell resolution improvement of 10x can be realized. The QIE is comprised of two key elements—a squeezed vacuum injector (SVI) that restores the high spatial frequencies lost by attenuation in soft-aperture entrance optics in the LADAR and a phase sensitive amplifier (PSA) that overcomes the inefficiency of the homodyne detector. When the QIE is combined with a phase-conjugate optical coherence tomographic (PC-OCT) technique for a two-fold range resolution enhancement, a 200-fold voxel (angle-angle-range) improvement is possible.

15. SUBJECT TERMS

LADAR, Quantum Image Enhancement, Phase Sensitive Amplification, Squeezed Vacuum Injection

16. SECURITY CLASSIFICATION OF:			**17. LIMITATION OF ABSTRACT**	**18. NUMBER OF PAGES**	**19a. NAME OF RESPONSIBLE PERSON** Donald J. Nicholson
a. REPORT U	**b. ABSTRACT** U	**c. THIS PAGE** U	UU	82	**19b. TELEPHONE NUMBER** *(Include area code)* N/A

Standard Form 298 (Rev. 8-98)
Prescribed by ANSI Std. Z39.18

ABSTRACT

The resolution of a homodyne LADAR can be enhanced significantly by applying quantum optical techniques in the receiver. This study, known as the Quantum Sensors Program, explored theoretically three types of quantum sensors, and developed two laboratory proof-of-concept demonstrations, one for angle-angle resolution improvement and the other for range resolution improvement. With a quantum image enhancer (QIE) inserted between the receive optics and the detector of a classical homodyne LADAR, an angular cell resolution improvement of 10x can be realized. The QIE is comprised of two key elements—a squeezed vacuum injector (SVI) that restores the high spatial frequencies lost by attenuation in soft-aperture entrance optics in the LADAR and a phase sensitive amplifier (PSA) that overcomes the inefficiency of the homodyne detector. When the QIE is combined with a phase-conjugate optical coherence tomographic (PC-OCT) technique for a two-fold range resolution enhancement, a 200-fold voxel (angle-angle-range) improvement is possible for a standoff homodyne LADAR. Underlying theory is established that relates the LADAR's signal-to-noise ratio (SNR) to its angular resolution. This modeling provides the framework within which various detection scenarios can be compared when resolving specular returns and fully-developed speckle scatter from a LADAR target. The efficacy of using non-classical light (a Type-1 sensor) for propagation to a target was shown to offer, at most, an inconsequential target-detection advantage for the highly-lossy scenarios associated with LADAR operation over 10-100 km standoff ranges. Several key no-go theorems were developed with respect to both Type-1 and Type-3 sensors. Two alternative quantum sensor categories—Type-2 using classical light with a non-standard receiver and Type-3 using transmitter-receiver entanglement—were studied theoretically. The approach employing a QIE for a Type-2 sensor was shown to present the most promise. The characteristics of the three types of sensors and a summary of salient theoretical results related to each type are presented. In addition, extensive modeling based on the developed theory show Type-2 sensor image improvement realized by employing SVI, PSA and combined SVI and PSA. Experimental results validating the QIE concept are shown using a PSA for angle image improvement and PC-OCT for two-fold range improvement, as well as for dispersion compensation. A Type-3 sensor technique, known as quantum illumination, was also studied theoretically and its application to secure communication briefly summarized. Ghost imaging applied to standoff sensing is examined and its underlying theory comprehensively explored. Finally, a conceptual design is introduced for a homodyne LADAR Type-2 sensor incorporating both PSA and SVI in a quantum-enhanced receiver.

TABLE OF CONTENTS

LIST OF FIGURES

EXECUTIVE SUMMARY

Conventional laser radar, or LADAR, has a spatial resolution that is restricted by the Rayleigh limit of its entrance pupil and its signal-to-noise ratio (SNR). In Phase I of the DARPA Quantum Sensors Program (QSP), researchers at Harris Corp., MIT, Northwestern University, University of Texas, Arlington, and BBN Technologies have shown — through extensive theory, modeling and proof-of-concept experiments — that quantum optical techniques can substantially improve the spatial resolution of such a sensor. As work progressed during Phase I of QSP, researchers focused on a LADAR design consisting of a soft-aperture, homodyne-reception system interrogating rough-surfaced targets whose returns exhibited fully-developed laser speckle. A coherent-state transmitter with a conventional homodyne receiver as a baseline LADAR sensor was augmented with squeezed-vacuum injection (SVI) at the soft aperture pupil to ameliorate the loss of high spatial-frequency information that this aperture induces. Because the standard Rayleigh-resolution criterion addresses the problem of distinguishing the presence of two point objects from the presence of one, decision theory was applied to obtain a quantitative performance comparison between conventional and SVI-augmented homodyne reception for such an idealized scenario. In particular, the spatial resolution was defined as the minimum angular separation between two speckle-return point targets at which the two targets can be distinguished from a single speckle-return point target within a specified error-probability bound. Furthermore, sub-unity detection efficiency was mitigated through the use of phase sensitive amplification (PSA) prior to detection. PSA gain overcomes the loss from inefficient detection and provides a substantial performance improvement, even without SVI, when detection efficiency is very low. Because LADARs are most frequently used to image complicated scenes, the modulation transfer function (MTF) behavior was derived for imaging extended speckle targets with the enhanced SVI plus PSA LADAR. Using an Air Force test pattern and a typical target scene, researchers performed computer simulations of conventional and quantum-enhanced imagery that illustrated the resolution enhancement of LADAR operation enabled by SVI, PSA and combined SVI plus PSA.

Theory developed during QSP Phase I can be distinguished by the taxonomy of three types of sensors based on whether or not the LADAR employs classical or non-classical light. A Type-1 sensor transmits non-classical light that is not entangled with the receiver. Theoretical no-go theorems for a Type-1 sensor were developed proving that the loss encountered in reasonable operational LADAR scenarios—1 to 100 km standoff distance—is so significant that there is virtually no advantage, as compared with a conventional classical-state LADAR, in using a non-classical transmitter state. For example, theory has shown that for a non-classical ten entangled photon *NOON* state used as a Type-1 sensor, typical losses introduce a prohibitively low probability of success (10^{-40}), leading to resolution capabilities below that of a classical sensor of equal power. In contrast, a Type-2 sensor transmits a classical state of light that is not entangled with the receiver, but employs a non-standard receiver, using quantum optical techniques, to gain its advantage over a classical LADAR. By using SVI and PSA in a quantum image enhancer (QIE), in conjunction with phase-conjugate optical coherence tomography (PC-

OCT), QSP researchers have theoretically confirmed that a potential 200-fold voxel (angle-angle-range volume) resolution improvement is possible. A Type-3 sensor transmits a state of light — either classical or non-classical — that is entangled with the LADAR receiver. One instantiation of this type of sensor, known as quantum illumination (QI), has been shown theoretically to enable a 6 dB error-exponent improvement in target detection performance, as well as improvement in one-versus-two point target resolution, when compared to a classical LADAR emitting identical optical power.

A number of variations of ghost imaging were explored and a comprehensive theoretical foundation established for several illumination scenarios. The salient features of a Gaussian-state analysis of ghost imaging are presented unifying prior work on biphoton and pseudothermal sources. Our analysis indicates that ghost-image formation is intrinsically due to classical coherence propagation, with the principal advantage afforded by the biphoton state being high-contrast imagery in the wideband limit. The Gaussian-state theory of pseudothermal ghost-image formation enabled the QSP theory group to identify two new configurations for lensless ghost imaging. First, theoretical results demonstrate that ghost imaging can be accomplished using a spatial modulator to create signal and reference beams with controlled spatial incoherence. The second configuration uses only one detector—a bucket detector—that collects a single pixel of light which has interacted with the object. This novel concept, referred to as computational ghost imaging, permits 3-D sectioning to be performed without a high spatial-resolution detector. .

In summary, theory pertaining to Type-1 sensors showed, via an encompassing no-go theorem, that propagation loss obviated any resolution improvement. A Type-3 sensor, known as QI, could produce a 6 dB error-exponent improvement for target detection in a lossy, noisy environment when operated in a low probability detect or low probability of intercept (LPD/LPI) mode. However, the benefit afforded by QI over a classical LADAR vanishes when the source power is allowed to be increased. For a Type-2 sensor concept developed during the QSP study, the foundation theory and the accompanying detailed modeling showed that 15 dB of SVI plus 15 dB of PSA (physically attainable values) can yield a 7-to-10-fold increase in the number of spatial resolution cells for a 25% detection efficiency compared with a Gaussian soft-aperture LADAR whose baseline SNR without SVI and PSA is 20 dB. Moreover, a proof-of-concept PSA experiment validated the concept that angle-angle improvement could indeed be realized. Furthermore, multiple spatial mode propagation theory corroborated the gains measured experimentally in the nonlinear crystals used for the PSA. By applying a technique known as phase-conjugate optical coherence tomography, QSP researchers experimentally demonstrated simultaneous two-fold range resolution improvement and propagation dispersion cancellation. Finally, a design concept was created for a quantum LADAR incorporating a QIE with conventional ranging that may be built in a future phase of the Quantum Sensors Program using present day squeezing and phase sensitive amplification apparatus and techniques.

1.0   INTRODUCTION

This report summarizes the fundamental theory for standoff quantum sensors and the experimental results from two complementary proof-of-concept laboratory demonstrations that validate the efficacy of using quantum optical techniques to enhance sensor resolution. Three types of sensors are defined theoretically based upon whether classical light or non-classical light is emitted by the sensor to interrogate the remote target. Under certain operating conditions, general theorems were proven which determine whether or not specific types of sensors could provide improved resolution when compared to classical Rayleigh resolution criterion. Results for a specific sensor – a LADAR operating at a range from the target as far as 1 to 100 km – emitting classical light but operating with a quantum image enhancer (QIE) in its receiver show theoretically that 10x resolution cell improvement in angle and a 2x improvement in range resolution can be realized with an overall voxel (angle-angle-range) improvement of 200x. This LADAR needs to operate with a soft aperture and employ homodyne detection to realize this resolution improvement.

The theoretical operating characteristics predicted for this homodyne LADAR were modeled and two experiments undertaken — one showing angle improvement and the other showing 2x range improvement. This remarkable improvement is achieved by two separate processes — a pair of functions that act in concert for angle improvement and a different function that effects improved range resolution. The angle resolution improvement is brought about by employing squeezed vacuum injection (SVI) to recover the high spatial frequency signal-to-noise ratio (SNR) lost from using a soft aperture and noiseless amplification by a phase sensitive amplifier (PSA) to overcome inefficiency in homodyne detection. The combined effects of SVI and PSA enable the QIE to provide the 10x cell image improvement. In a separate operation, range resolution is improved by using a phase-conjugate optical coherence tomography (PC-OCT) technique.

As a first step in quantifying the characteristics of a quantum enhanced LADAR, a taxonomy of three types of sensors was established: Type-1 in which the emitted light is non-classical and not entangled with the receiver; Type-2 in which the emitted light is classical and not entangled with the receiver but quantum enhancement is applied in the receiver; and Type-3 in which the emitted light is classical or non-classical but entangled with light retained by the LADAR. Theorems bounding the operating characteristics of these Type-1 and Type-3 sensors are presented in the first technical discussion (Section 2.0) of this report summarizing theoretical and modeling results.

To supplement the theoretical work, a second essential portion of this study refines the concept of resolution and connects SNR of the LADAR with its operating angular resolution. This refinement establishes the baseline against which quantum enhanced performance can be compared, and its details are contained in the theory section. To demonstrate clearly the resolution improvement afforded by SVI plus PSA Type-2

quantum sensing, a hypothesis testing scenario is analyzed in which the target return is equally likely to be from an on-axis point target or from two equal-strength point targets placed symmetrically about the optical axis. With a likelihood-ratio test, the minimum error probability decision rule is derived and its error probability calculated as a function of the angular separation between the two targets and the signal-to-noise ratio. The scaling of the resolution with SNR will be presented in detail in the modeling portion of the theory section. Specifically, improvements with SVI, PSA, and combined SVI and PSA are presented for a homodyne LADAR Type-2 sensor with a detection efficiency of 0.25. The hypothesis-testing resolution analysis is supplemented with image simulations based on the modulation transfer function (MTF) and noise spectral density of the baseline and quantum-enhanced sensors. MATLAB$^{®}$ simulations establish the subjective imaging benefits afforded by SVI plus PSA when viewing a speckle-limited USAF test target pattern. Moreover, the simulations confirm the resolution predictions found for the point-target hypothesis testing problem.

For completeness, the theory section includes a discussion of ghost imaging, for this technique often is included in the broader context of quantum enhanced imagers. A number of variations of ghost imaging are explored and a comprehensive theoretical foundation established for several illumination scenarios. The salient features of a Gaussian-state analysis of ghost imaging are presented unifying prior work on biphoton and pseudothermal sources. Our analysis indicates that ghost-image formation is intrinsically due to classical coherence propagation, with the principal advantage afforded by the biphoton state being high-contrast imagery in the wideband limit. The Gaussian-state theory of pseudothermal ghost-image formation enabled our QSP theory group to identify two new configurations for lensless ghost imaging. First, theoretical results demonstrate that ghost imaging can be accomplished using a spatial modulator to create signal and reference beams with controlled spatial incoherence. The second configuration uses only one detector—a bucket detector—that collects a single pixel of light which has interacted with the object. This novel concept, referred to as computational ghost imaging, permits 3-D sectioning to be performed without a high spatial-resolution detector.

Extensive work is presented on a particular Type-3 sensor known as quantum illumination (QI), because it affords a 4-fold improvement in target-detection error exponent, in comparison with a conventional LADAR of the same transmitter power, despite the destruction of its entanglement by channel loss and noise. The interest in this type of sensor transcends that of a classical standoff LADAR with applications to low probability of intercept and low probability of detect (LPI/LPD) scenarios wherein operation would be low signal level transmission in a noisy background and for secure communications such as encountered with quantum key distribution (QKD). The theoretical results and key theorems are discussed, as well as the supporting modeling that illustrates the SNR improvement.

The Type-2 LADAR theory and modeling presented in this report assume a planar target at known range with emphasis placed on the enhancement of angular resolution provided by SVI and PSA in a soft-aperture LADAR. In addition, the theory and modeling are based on a squeezed-vacuum source and phase-sensitive amplifiers that are assumed to be continuous-wave (cw) pumped devices. Details of key theorems that are discussed in the theory section or referenced team memoranda that have not been formally published are included in the appendix.

Following the theory and modeling section, Sections 3.0 and 4.0 present data from the two key proof-of-concept experiments that were performed during this program. The results from these proof-of-concept experiments show the angle resolution improvement brought about by using the PSA portion of the QIE and the two-fold range resolution improvement via PC-OCT. Additionally, the PC-OCT experiment also showed definitive dispersion compensation. Although the quantum enhanced concept reported here can be applied to any soft-aperture, homodyne LADAR operated at any wavelength within a large portion of the electromagnetic spectrum, all experimental work was undertaken at 1.55 μm to take advantage of several pieces of key equipment and available lasers.

A summary of PSA experimental results and the accompanying theory of multimode image amplification are presented in Section 3.0. Data are presented which corroborate the PSA gain as a function of pump power of the nonlinear crystal. A three dimensional numerical model, developed during the program, uses a split-step Fourier method whose results show good quantitative agreement with the experimental data. Just as important, the model predicts an optimum input signal phase profile for image amplification in a PSA with a finite-size pump beam.

Section 4.0 of this report summarizes the experimental results demonstrating a two-fold improvement in range resolution by using PC-OCT. Data are also presented definitively demonstrating dispersion compensation using the PC-OCT technique. Although dispersion is unlikely to be a problem for standoff sensors operating over terrestrial paths with picosecond pulses at 1.55 μm wavelengths, the compensation technique could be applicable at shorter pulsewidths or longer wavelengths.

A possible quantum Type-2 LADAR concept is introduced in Section 5.0. This LADAR would combine both SVI and PSA for angle-angle resolution improvement but would employ a classical range detector because the transverse resolution is the more important enhancement desired by the coherent LADAR community. Development of this concept is envisioned for a follow-on effort.

Finally, the salient results of the report are summarized in Section 6.0, and some of the risks that need to be addressed in more detail in the future are outlined. This report should provide a solid theoretical foundation for applying quantum optics to enhance the resolution of a LADAR operated as a standoff sensor. Additional investigation beyond this 18-month study would be necessary to build a more comprehensive picture of the complete application of quantum optics to sensors.

2.0   THEORY AND MODELING FOR QUANTUM IMAGING

Phase I of the DARPA Quantum Sensors Program had, as its principal goal, developing the underlying theory — and supporting modeling — that would demonstrate the possibility of building an imaging sensor whose performance exceeded the Rayleigh resolution limit by a factor of ten (or more) through the use of quantum mechanical resources. Proof-of-principle experiments in support of the core theory work were also possible, but not meant to be the focus of Phase I. For its baseline sensor the Harris team chose a soft-aperture LADAR system, imaging spatially-resolved targets at ranges from 1 to 100 km, see Figure 1.
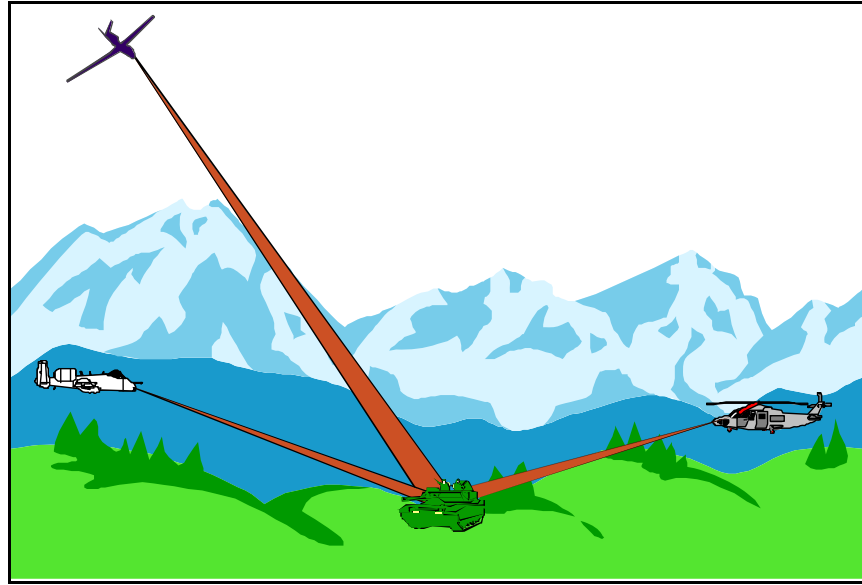
Figure 1: LADAR Standoff Sensing

To beat the Rayleigh limit on angular resolution, the Harris team augmented its baseline LADAR receiver with a quantum image enhancer, comprised of squeezed-vacuum injection (SVI) plus phase-sensitive amplification (PSA), see Figure 2.
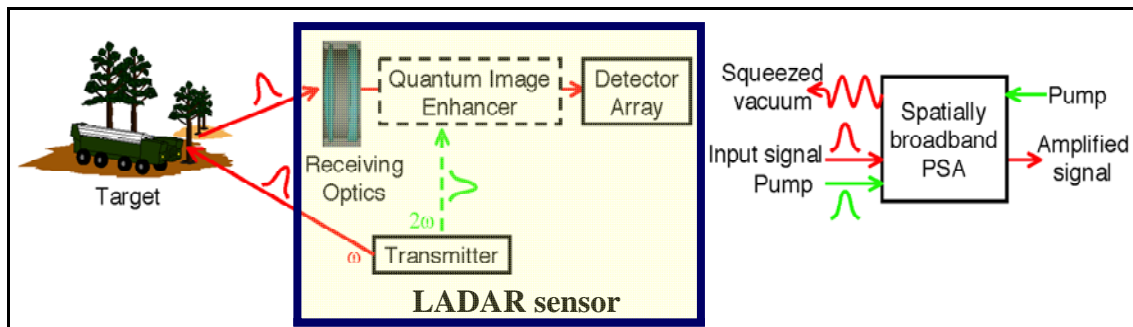
Figure 2: QSP baseline and quantum enhanced LADAR

The QSP study combined improved angular resolution with improved range resolution through use of phase-conjugate ranging, see Figure 3. Because the fundamental theory of phase-conjugate ranging had been established in earlier work [1] by members of the QSP effort, and because beating the Rayleigh limit was the *sine qua non* criterion for initiation of a Phase II program, the QSP theory and modeling effort concentrated on quantifying the angular resolution limit in its baseline LADAR concept and demonstrating that its SVI plus PSA quantum-image enhancer did lead to a 10-fold improvement in resolution on a pixel basis.
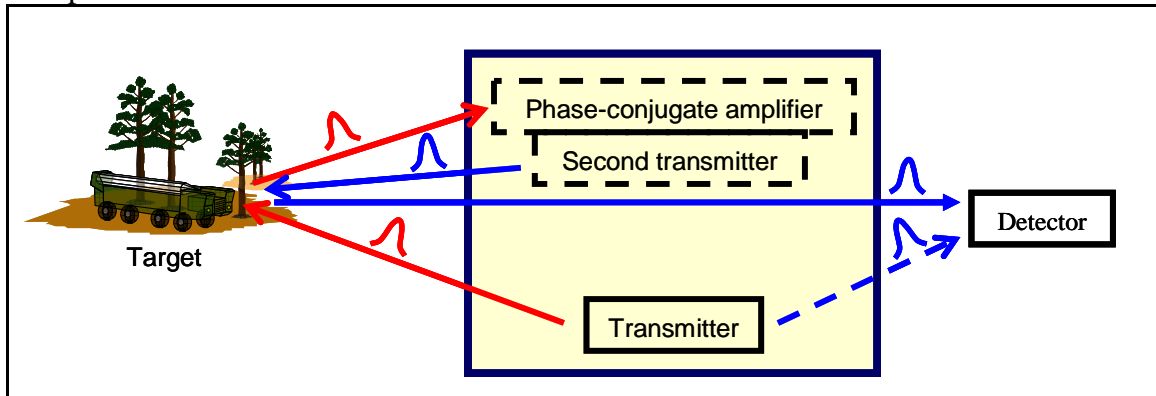
Figure 3: LADAR system for phase-conjugate ranging

However, in order to fully explore the possibilities afforded by quantum mechanical resources in imaging scenarios, the Harris team also developed and instantiated a taxonomy for quantum imaging. The quantum-enhanced sensor from Figure 2 is a Type-2 system, in this taxonomy, because its transmitter employs classical-state (laser) light that is not entangled with the quantum state of the receiver, and the receiver employs non-classical resources to achieve its resolution enhancement over the baseline sensor. However, even before embarking on a comprehensive theory for quantum imaging, a careful definition of what constitutes quantum imaging is essential. That definition, and the quantum imaging taxonomy that follows there from, will be the first topic we will address in this section of the report.

2.1 Quantum Imaging Taxonomy

All optical imaging is quantum, regardless of whether it is performed passively, using natural illumination, or actively, with laser light in a LADAR system. This is so because light is quantum mechanical and photodetection is a quantum measurement. However, the Harris team believes that a clear distinction can and must be drawn between imaging systems — LADAR systems, in the case of our Quantum Sensors Program effort — that *require* quantum mechanical descriptions as opposed to those for which a quantitatively identical characterization can be obtained from semiclassical photodetection theory. In semiclassical photodetection theory light is treated as a classical (possibly stochastic) electromagnetic field and the fundamental noise encountered in photodetection is the shot noise associated with the discreteness of the electron charge. It has long been known that light beams whose quantum states are Glauber coherent states or classically-random

mixtures thereof have quantum photodetection statistics — for the three standard photodetection configurations, viz., direct, homodyne, and heterodyne detection — that coincide with those obtained from semiclassical theory. The Harris baseline sensor, which will be described in greater detail below, is thus a classical imager because its performance can be correctly calculated from semiclassical photodetection theory. More generally, semiclassical analysis is sufficient to quantify LADAR performance when all of the following conditions are met:

- The quantum state of the light radiated by the transmitter is classical.
- Electromagnetic propagation to and from the target is linear, i.e., characterized by linear diffraction integrals.
- The target interaction is linear, e.g., reflection from a planar object as represented by a multiplicative field-reflection coefficient.
- The receiver uses direct, homodyne, or heterodyne detection.

The LADAR scenario shown in Figure 1 is one in which both the propagation and target interaction will be linear. Thus, for a LADAR system to be a quantum imager — as opposed to one for which semiclassical analysis suffices — it must either employ a non-classical state transmitter, or use a non-standard receiver, or both. The Harris team refined the description of quantum imagers into the following trichotomy.

- Type-1 sensors: A Type-1 sensor transmits a non-classical state that is not entangled with the receiver.
- Type-2 sensors: A Type-2 sensor transmits a classical state that is not entangled with the receiver and employs a non-standard (quantum-enhanced) detection procedure in that receiver.
- Type-3 sensors: A Type-3 sensor transmits a state — which may be classical or non-classical — that is entangled with the receiver.

The Harris team expended its theory effort on topics concerning all three components of this quantum imaging taxonomy. The bulk of the effort was devoted to the SVI plus PSA Type-2 sensor shown in Figure 2. However, considerable work established theorems and determined practical limitations on the potential offered by Type-1 and Type-3 sensors. In addition, we identified possible performance advantages afforded by quantum illumination — a novel class of Type-3 systems— in target detection, point-target resolution, and secure communication applications. We also investigated ghost imaging systems, because prior work by some of our team members had determined the boundary between the classical and quantum versions of this sensor class [2], and we were well positioned to extend prior work to a full understanding of ghost imaging's capabilities.[1]

---

[1] Ghost imaging had been proposed by another Quantum Sensors Program contractor, and the Harris team investigated its potential because several Harris team members had substantial prior experience with ghost imaging.

2.2 No-Go Theorems for Type-1 and Type-3 Sensors

At the outset of our theoretical work we chose a Type-2 sensor for our approach to beating the Rayleigh resolution limit. This choice was firmly grounded in a basic fact of life for LADAR imaging in the Figure 1 scenario: the transmitter-to-target-to-receiver path is exceedingly lossy. In particular, we noted the following characteristics of such an imager

- The diffraction-limited spot produced by realistic transmitter optics spatially resolves targets of interest. Thus, the free-space transmitter-to-target loss is negligible.
- Clear-weather extinction loss in the atmosphere — due to absorption and scattering — is not problematic, with loss coefficients of 0.5 to 1 dB/km being typical.
- Target reflectivity is reasonable, with 10% being a typical value.
- Targets of interest have surfaces that are quite rough on the scale of LADAR wavelengths making their reflection patterns quasi-Lambertian and the target-to-receiver loss very high.

Quasi-Lambertian target reflection leads to the high loss. For example, with a 10-cm-diameter receiver pupil collecting light from a target that is 10 km away, the loss due to quasi-Lambertian reflection is approximately 100 dB. Non-classical light states — such as number states, squeezed states, and $N00N$ states — suffer catastrophic degradation of their advantageous non-classical characteristics in such high-loss environments. Hence the Harris team sought general no-go theorems for Type-1 and Type-3 sensors that might show they had little or no advantage in LADAR applications when compared to classical baseline systems. Here we shall summarize the key results we derived from such studies; for proofs and additional details see [3]-[5].

Consider the task of detecting a non-fluctuating point target of known reflectivity that may, or may not; be present in a particular azimuth-elevation-range bin. Assume that this target is equally likely to be absent or present, and that the radar interrogates the chosen azimuth-elevation-range bin with M optical modes whose transmitter-to-target-to-receiver coupling coefficients are $\{\kappa_m : 1 \leq m \leq M\}$ arranged in decreasing order. Then, if the transmitter is constrained to use at most N_S photons on average and there is no noise in the propagation channel, the error probability of a system that uses the optimum non-classical transmitter state, in conjunction with the minimum error probability receiver for the resulting target return, satisfies

$$\Pr(e) \geq \frac{1 - \sqrt{1 - e^{-\kappa_1 N_S / (1 - \kappa_1)}}}{2}. \tag{1}$$

This lower bound should be compared with the following upper bound on the error probability of an optimized classical system that uses coherent-state (laser) light of the same average photon number,

$$\Pr(e) \leq \frac{1 - \sqrt{1 - e^{-\kappa_1 N_S}}}{2}. \tag{2}$$

Equations (1) and (2) reveal that the maximum performance improvement to be expected from use of a Type-1 quantum sensor in this highly idealized situation will be inconsequential when 100 dB loss is involved, i.e., when $\kappa_1 \approx 10^{-10}$.

We have recently extended the preceding no-go result to Type-3 sensing when the transmitter employs signal-number diagonal (SND) states [4]. The task is still to detect a non-fluctuating point target of known reflectivity that is equally likely to be present in or absent from a particular azimuth-elevation-range bin. The Type-3 sensor's transmitter produces the M-mode-pair pure state[2]

$$|\psi> = \sum_{\mathbf{n}} \psi_{\mathbf{n}} |\mathbf{n}>_S |\mathbf{n}>_I, \tag{3}$$

where $|\mathbf{n}>_K \equiv |n_1, n_2, ..., n_M>_K$ for $K = S, I$ is the M-mode number state for its signal (S) and idler (I) beams. The transmitter uses the signal beam to interrogate the chosen azimuth-elevation-range bin, and retains the idler beam for a minimum error probability joint quantum measurement with the light returned from that bin. Suppose, as before, that the transmitter-to-target-to-receiver coupling coefficients are $\{\kappa_m : 1 \leq m \leq M\}$ arranged in decreasing order, the transmitter is constrained to use at most N_S photons on average in the signal beam, and there is no noise in the propagation channel. Then it turns out that the optimum joint quantum measurement for the SND Type-3 sensor yields an error probability that is again bounded from below by the expression given in Eq. (1). Thus, as in the case of Type-1 sensing, there is virtually no value to using SND Type-3 sensing in this highly idealized situation, i.e., for typical LADAR scenarios a coherent-state (laser) transmitter of the same average photon number gives essentially the same performance.

---

[2] Instead of $\{|\mathbf{n}>_I\}$, the SND transmitter could employ any M-mode orthonormal basis for its idler states without changing the results of our analysis.

We obtained more elaborate and more useful no-go results from our classicalization theorem.

> *Theorem (Classicalization):* Suppose that $\hat{\rho}_{\text{in}}$ is an arbitrary *M*-mode density operator at the input to a linear optical channel with modal transmissivities $\{\kappa_m : 1 \le m \le M\}$ and independent, identically-distributed, zero-mean, isotropic-Gaussian modal noises with average photon numbers $\{N_m : 1 \le m \le M\}$. Then the resulting output density operator, $\hat{\rho}_{\text{out}}$, will be a classical state if $N_m \ge \kappa_m$ holds for $1 \le m \le M$.

Now consider a Type-1 LADAR system that transmits the state $\hat{\rho}_{\text{in}}$. Because background light at the eye-safe 1.55 μm wavelength is an isotropic Gaussian noise with average photon number per mode that will typically exceed the transmitter-to-target-to-receiver transmissivities, we see that the receiver will be observing a classical state, regardless of how non-classical the transmitter's output may have been. Furthermore, applying the classicalization theorem at the transmitter shows that the addition of isotropic-Gaussian noise with an average of one photon per mode will transform $\hat{\rho}_{\text{in}}$ into a classical state $\hat{\rho}_{\text{in}}^c$ whose corresponding output state — after lossy, noisy propagation — will be denoted $\hat{\rho}_{\text{out}}^c$. In terms of $\{\hat{\rho}_{\text{in}}, \hat{\rho}_{\text{out}}; \hat{\rho}_{\text{in}}^c, \hat{\rho}_{\text{out}}^c\}$ we have proven the following theorem bounding the difference in quantum measurement statistics resulting from LADAR transmission of $\hat{\rho}_{\text{in}}$ versus LADAR transmission of $\hat{\rho}_{\text{in}}^c$.

> *Theorem (Quantum Measurement Bound):* Let x be the outcome of an arbitrary quantum measurement made at the LADAR receiver, and let $\Pr(x \in X \mid \hat{\rho})$ be the probability that this outcome lies in the set *X* when the LADAR's transmitter state was $\hat{\rho}$. Then we have that
>
> $$\left| \Pr(x \in X \mid \hat{\rho}_{\text{in}}) - \Pr(x \in X \mid \hat{\rho}_{\text{in}}^c) \right| \le 2 \sum_{m=1}^{M} \sqrt{\frac{N_m}{N_m + 1}}, \qquad (4)$$
>
> when the channel noise is sufficient to classicalize $\hat{\rho}_{\text{out}}$.

At this point, our no-go theorem for Type-1 sensing follows immediately from classicalization and the quantum measurement bound.

> *Theorem (Type-1 No-Go):* Let $\hat{\rho}_{\text{in}}$ be an *M*-mode non-classical input state for a LADAR system and let $\hat{\rho}_{\text{in}}^c$ be its classicalization. Suppose that $\hat{\rho}_{\text{in}}$ has average modal photon numbers $N_{S_m} \gg 1$ for $1 \le m \le M$ and that the transmitter-to-target-to-receiver transmissivities and isotropic-Gaussian modal noise strengths satisfy $\kappa_m \le N_m \ll 1$ for $1 \le m \le M$. Furthermore, assume that *M* is sufficiently small

that $\varepsilon \equiv 2\sum_{m=1}^{M}\sqrt{\dfrac{N_m}{N_m+1}} << 1$ prevails. Then, the following conditions hold simultaneously:

- $\left| \text{tr}\left(\hat{\rho}_{\text{in}}^{c} \sum_{m=1}^{M} \hat{N}_{S_m} \right) - \text{tr}\left(\hat{\rho}_{\text{in}} \sum_{m=1}^{M} \hat{N}_{S_m} \right) \right| << \text{tr}\left(\hat{\rho}_{\text{in}} \sum_{m=1}^{M} \hat{N}_{S_m} \right)$ (5)

- $\left| \Pr(x \in X \mid \hat{\rho}_{\text{in}}) - \Pr(x \in X \mid \hat{\rho}_{\text{in}}^{c}) \right| \leq \varepsilon,$ (6)

where $\left\{ \hat{N}_{S_m} : 1 \leq m \leq M \right\}$ are the modal photon-number operators at the LADAR transmitter and x is the outcome of an arbitrary quantum measurement made at the LADAR receiver.

The physical import of the Type-1 No-Go Theorem is simple. Suppose its premises are satisfied. Then, for any non-classical input state at the LADAR transmitter and any quantum measurement made at the LADAR receiver the classicalization of that transmitter state entails a negligible increase in the transmitter's total average photon number and it results in a negligible change in the receiver's quantum-measurement statistics. In short, there is essentially nothing to be gained, in this Type-1 scenario, from use of quantum resources.

We have also obtained the following no-go theorem for Type-3 quantum sensing.

Theorem (Type-3 No-Go):   Let $\hat{\rho}_{\text{in}}$ be a two-mode non-classical state characterizing the signal and idler modes at the LADAR transmitter, with each having average photon number $N_S >> 1$, and let $\hat{\rho}_{\text{in}}^{c}$ be the classicalization of $\hat{\rho}_{\text{in}}$. Suppose that the idler is retained in a lossless, noiseless manner at the LADAR but the signal is used to interrogate a target over a lossy (transmissivity $\kappa << 1$), very noisy (isotropic-Gaussian noise with average photon number $N >> 1$) transmitter-to-target-to-receiver channel. Then, if the channel is such that joint state, $\hat{\rho}_{\text{out}}$, of the target return and the idler is classical, we have that the following conditions hold simultaneously:

- $\left| \text{tr}\left(\hat{\rho}_{\text{in}}^{c} \hat{N}_{S} \right) - \text{tr}\left(\hat{\rho}_{\text{in}} \hat{N}_{S} \right) \right| << \text{tr}\left(\hat{\rho}_{\text{in}} \hat{N}_{S} \right)$

    (7)

1.0 $\left| \Pr(x \in X \mid \hat{\rho}_{\text{in}}) - \Pr(x \in X \mid \hat{\rho}_{\text{in}}^{c}) \right| \leq 2\kappa / N << 1$

(8)

where $\hat{N}_S$ is the signal-mode photon-number operator at the LADAR transmitter and x is the outcome of an arbitrary joint quantum measurement — on the target return and the idler — made at the LADAR receiver.

Our Type-3 No-Go Theorem shows that the performance obtained in two-mode Type-3 quantum sensing is closely approximated — under the theorem's premises — by that of a classicalized transmitter of essentially the same average transmitted photon number as the non-classical source.

We shall revisit no-go theorems in Section 2.4.4, where we shall apply practical implementation considerations to lift the limitations of high-brightness, low-to-modest mode number that were required in the no-go theorems we have just presented.

2.3 Imaging with Squeezed-Vacuum Injection and Phase-Sensitive Amplification

The Harris team for the DARPA Quantum Sensors Program (QSP) chose to concentrate its Phase I efforts on the Type-2 quantum sensor shown in Figure 2 for improving the angular resolution of a classical-state baseline LADAR system. In Type-2 quantum sensing, the transmitter emits a classical state — laser light — that is not entangled with any residual state left behind in the LADAR system. The system then employs a non-standard receiver — something other than ordinary heterodyne, homodyne, or direct detection — in which quantum effects provide enhanced angular resolution.

In the baseline sensor, a laser transmitter illuminates the target region and the return from that region is collected by a soft-aperture entrance pupil and focused onto a homodyne detection array. The same transmitter and homodyne detection array is used in the Harris team's Type-2 quantum sensor, with a quantum image enhancer inserted between the entrance pupil and detector array. The quantum image enhancer (QIE) employs spatially-broadband squeezed-vacuum injection (SVI) at the entrance pupil to mitigate the loss of high spatial-frequency information that the baseline sensor incurs from soft-aperture attenuation. The QIE also uses spatially-broadband phase-sensitive amplification (PSA) immediately before the homodyne array to compensate for low efficiency — the combination of mixing and quantum efficiency — in that homodyne detection process. The Harris team's Phase I analysis and modeling have shown that the Type-2 sensor sketched in Figure 2 satisfies all the DARPA Quantum Sensor Program's metrics for initiation of a Phase II program. In this section we shall present a brief summary of those results, concentrating on the improvement in angular resolution when imaging a target in a single range bin.

2.3.1 System Configuration and Angular Resolution Analysis.

The classical target-return complex-field envelope impinging on the soft-aperture entrance pupil of the LADAR receiver from a planar object located L meters away in the free-space[3] Fraunhofer zone is given by

$$E_R(\vec{\rho},t) = \int \sqrt{E_T}\, s(t - 2L/c)\, \xi_T(\vec{\rho}')\, T(\vec{\rho}') \frac{e^{-jk\vec{\rho}\cdot\vec{\rho}'/L + jk|\vec{\rho}|^2/2L}}{j\lambda L}\, d\vec{\rho}', \qquad (9)$$

where: E_T is the energy in the transmitted pulse (measured, for convenience, in units of the photon energy at the operating wavelength λ); $s(t)$ is the normalized baseband shape of the transmitter pulse; c is the speed of light; $\xi_T(\vec{\rho}')$ is the normalized transmitter beam pattern at the target plane; $T(\vec{\rho}')$ is the target's field-reflection coefficient; the remainder of the integrand is the Fraunhofer diffraction kernel with $\vec{\rho}$ and $\vec{\rho}'$ being 2-D vectors in the receiver's entrance pupil and on the target plane, respectively; and we have omitted an unimportant absolute-phase factor.

In the baseline sensor, the target-return field passes through a soft-aperture pupil,[4] $P(\vec{\rho}) = e^{-2|\vec{\rho}|^2/R^2}$, and is then focused onto a homodyne-detector array. Equation (9) shows that the pupil-plane target-return field contains the spatial Fourier transform of the illuminated portion of the target's field-reflectivity coefficient. Thus the soft-aperture attenuation suppresses information about the target's high spatial-frequency components, hence limiting the LADAR's angular resolution. In particular, when homodyne detection of the real quadrature of the focal-plane illumination is performed — using a spherical-wave local oscillator on a continuum photodetector array — followed by post-detection matched filtering in the time domain, the result is a spatial random process

$$y_r(\vec{\rho}) = \mathrm{Re}\left(\sqrt{\eta} \int \sqrt{E_T}\left(\frac{\sqrt{\pi R^2}}{2\lambda L} \right) \xi_T(\vec{\rho}')\xi_P(\vec{\rho} - \vec{\rho}')T(\vec{\rho}')\,d\vec{\rho}' \right) + n_r(\vec{\rho}), \qquad (10)$$

where we have corrected for image inversion, used a normalization convention that is convenient for the quantum case that will follow, defined η to be the receiver's homodyne efficiency and again suppressed an unimportant absolute-phase factor. The first term in Eq. (10) contains the target image with

---

[3] For terrestrial application scenarios, in which atmospheric turbulence is neglected, this diffraction formula should be augmented with an atmospheric extinction term to account for absorption plus scattering loss.

[4] The Harris team's Phase I analysis assumed a Gaussian-pupil soft aperture, although other choices are certainly possible.

$$\xi_P(\vec{\rho}) = \frac{\sqrt{\pi R^2}}{\lambda L} e^{-k^2 |\vec{\rho'}|^2 R^2 / 8L^2} \qquad (11)$$

being the normalized target-plane antenna pattern associated with the soft-aperture homodyne system. The second term, $n_r(\vec{\rho})$, is a zero-mean, real-valued, white Gaussian noise process with spectral density 1/4. It is the whiteness of the measurement noise in the homodyne array — in conjunction with the loss of high-spatial frequency target information in passage through the soft-aperture entrance pupil — that limits the baseline LADAR's angular resolution.

Performance analysis for the baseline LADAR can be accomplished within the construct of semiclassical photodetection theory, even though light is really quantum mechanical and photodetection is a quantum measurement. In semiclassical theory, light is treated as a classical (possibly stochastic) electromagnetic field, and the discreteness of the electron charge leads to shot noise as the fundamental noise in high-sensitivity photodetection. Consequently, the semiclassical theory interprets the noise term in Eq. (10) as the shot noise of the strong local oscillator used in the homodyne process. It has long been known, however, that semiclassical photodetection theory is quantitatively correct when the quantum state of the illumination falling upon the detector is a Glauber coherent state or a classically-random mixture of such states. Laser light is a classical state, so semiclassical theory does, indeed, suffice to treat our baseline sensor *quantitatively*. The key to Type-2 quantum sensing is the *qualitative* difference between the semiclassical and quantum theories of homodyne detection. In the quantum treatment of our baseline sensor, the noise in Eq. (10) consists of three components: quadrature quantum noise from the target return, plus vacuum-state quantum noise associated with the attenuation incurred at the soft aperture, plus vacuum-state quantum noise associated with inefficient ($\eta < 1$) homodyne detection. As shown in Figure 4, the use of squeezed-vacuum injection and phase-sensitive amplification can *reduce* the noise level in which the image term in the homodyne output is embedded. Specifically, using spatially-broadband SVI with squeeze parameter r and spatially-broadband PSA with quadrature-power gain G_{eff} the quantum image enhancer changes Eq. (10) into

$$y_r(\vec{\rho}) = \mathrm{Re}\left(\sqrt{\eta G_{\mathrm{eff}}} \int \sqrt{E_T} \left(\frac{\sqrt{\pi R^2}}{2\lambda L} \right) \xi_T(\vec{\rho'}) \xi_P(\vec{\rho} - \vec{\rho'}) T(\vec{\rho'}) d\vec{\rho'} \right) + n_r(\vec{\rho}), \qquad (12)$$

where $n_r(\vec{\rho})$ is now a zero-mean, real-valued Gaussian random process with spectral density

$$S_{n_r n_r}(\vec{f}) = \frac{\eta G_{\mathrm{eff}}}{4} \left(|P(\lambda L \vec{f})|^2 + (1 - |P(\lambda L f)|^2) e^{-r} \right) + \frac{1 - \eta}{4}. \qquad (13)$$

14

The first term in parentheses in Eq. (13) is the quantum noise contributed by the target-return light. The second term in parentheses is the quantum noise that is due to the squeezed-vacuum injection ($r > 0$ is the squeeze parameter). The term outside the parentheses is the quantum noise contributed by the sub-unity homodyne efficiency.
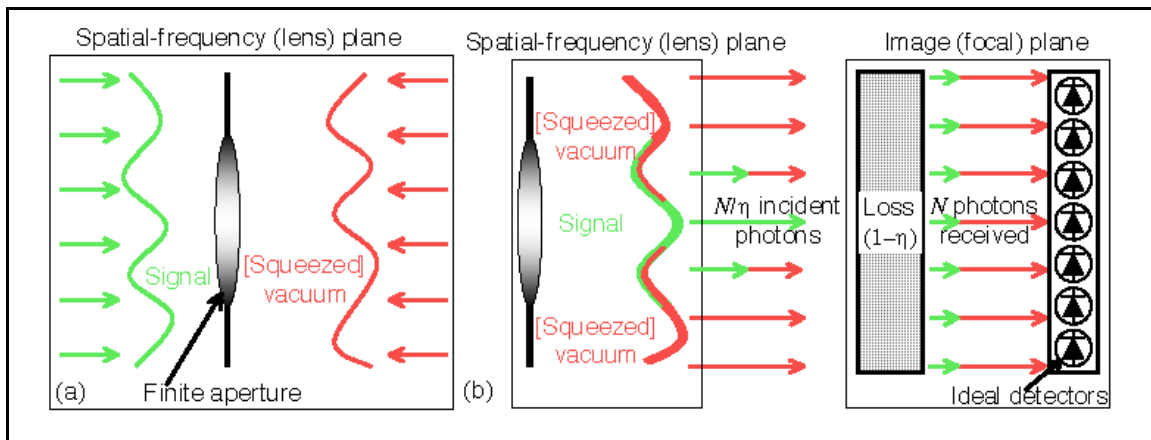
Figure 4: Notional schematic of squeezed-vacuum injection plus phase-sensitive amplification, viz., the quantum image enhancer block from Figure 2

When $G_{\text{eff}} = 1$ and $r = 0$, there is neither phase-sensitive amplification nor squeezed-vacuum injection and Eq. (13) reduces to the noise spectrum of the baseline sensor. However, with $r > 0$, the noise injected by the soft-aperture attenuation at high spatial frequencies is reduced. Furthermore, with $G_{\text{eff}} > 1$, the significance of the noise injected by sub-unity homodyne efficiency is reduced. Together, they provide quantum image enhancement in that the attenuated high spatial-frequency components of the image-bearing term in Eq. (12) are more readily discernible from this reduced noise level.

To clearly demonstrate the resolution improvement afforded by SVI plus PSA Type-2 quantum sensing, the Harris team analyzed a hypothesis testing scenario in which the target return was equally likely to be from an on-axis point target or from two equal-strength point targets placed symmetrically about the optical axis. For the assumed Gaussian soft-aperture pupil function, the Rayleigh-resolution angle is $\theta^{(\text{Ray})} = 0.6\lambda/R$. We considered targets that gave specular returns and those that gave fully-developed speckle returns, concentrating on the latter because they are more appropriate to LADAR wavelengths ($\lambda \approx 1\,\mu\text{m}$) owing to the quasi-Lambertian reflection from typical targets. Using a likelihood-ratio test, we derived the minimum error probability decision rule and calculated its error probability as a function of the angular separation between the two targets and the signal-to-noise ratio (SNR).[5] Details of our derivations can be found in [6]-[8]. Angular resolution was then defined to be the angular separation at which the

---

[5] SNR is defined to be the average number of detected signal photons in the measurement interval, even when we consider the quantum enhancement provided by SVI and PSA. Both target hypotheses are assumed to give the same SNR.

error probability fell below a chosen threshold value (0.03 in the figures that follow). Figure 5 shows an example of the speckle-target results that we have obtained, see [9],[10] for more details. The black dots in this figure plot the resolution angle for the baseline sensor, with η = 0.25 homodyne efficiency, as a function of the SNR, for the baseline sensor. The green dots in Figure 5 show an SVI-enhanced receiver and the pink dots show an SVI+PSA enhanced receiver. The unresolved regions in Figure 5 refer to regimes in which the resolution diverges. At high SNR values this resolution scales as $\theta^{(Res)} \propto SNR^{-3/10}$. Angular resolution diverges below a threshold SNR, 20 dB in this example, because the signal energy is then insufficient to discriminate between the one-target and two-target hypotheses, regardless of the angular separation of the latter.
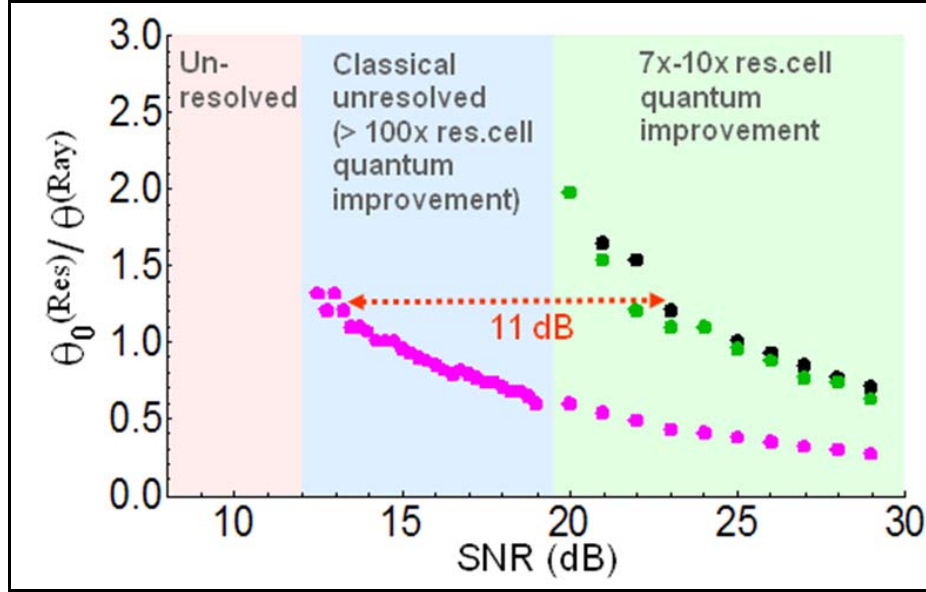
Figure 5: Normalized angular resolution versus SNR for $\eta = 0.25$ homodyne efficiency

To assess the resolution improvement afforded by the proposed SVI+PSA Type-2 sensor, we then analyzed a LADAR enhanced by SVI and PSA in this same formalism. The green dots in Figure 5 show the case of $\eta = 0.25$ homodyne efficiency with 15 dB of SVI but no PSA. The low homodyne efficiency contributes a large amount of vacuum-state quadrature noise that kills the advantage offered by SVI. The pink dots show the case in which there is 15 dB of SVI *and* a 9.3 dB PSA gain G.[6] In this case, one sees a significant improvement in the resolution at all SNR values. Moreover, when 12 dB < SNR < 20 dB, the baseline sensor's resolution diverges, whereas the SVI plus PSA quantum sensor maintains very good resolution.

The angular resolution improvement provided by the Harris team's Type-2 quantum sensor can be quantified by considering the effective shift in SNR of the resolution curve relative to that of the classical baseline sensor. For the example plotted in Figure 5, this SNR shift is 11.5 dB. To obtain a systematic understanding of this angular resolution improvement, we calculated the SNR shift for several values of η and the PSA gain G. Figure 6 shows, as expected, that SVI alone only gives a significant SNR shift at high values of the homodyne efficiency. As η decreases, the SVI-only system loses its advantage (green curve), but this advantage is restored when PSA is used in conjunction with SVI. In the limit of very low η the improvement is largely governed by the PSA gain, which can, in principle, shift the SNR curve by up to $1/\eta$ (black curve).
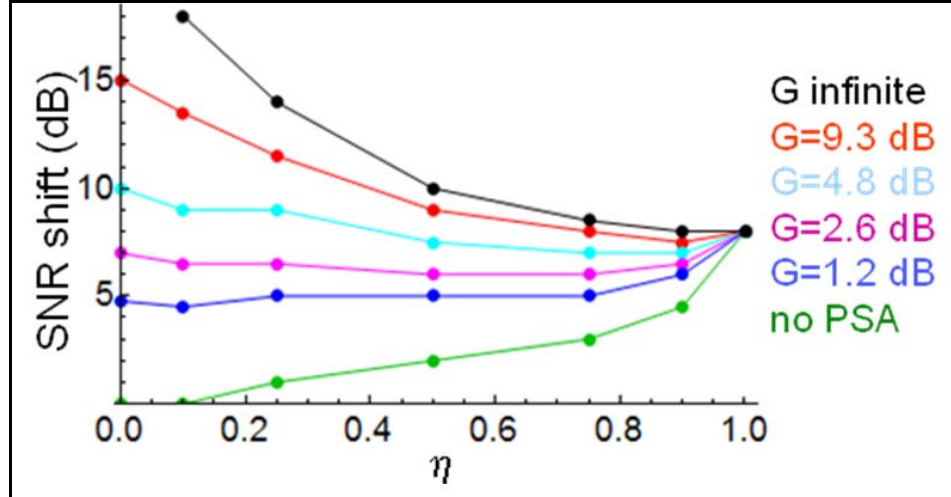
Figure 6: Effective SNR shift (relative to the baseline sensor) for 15 dB SVI plotted versus homodyne efficiency η for various values of the PSA gain G

---

[6] Strictly speaking, G is the gain of the PSA device when it is used as a phase-insensitive amplifier, but we will refer to it as the PSA gain. In terms of G, we have that the PSA quadrature power gain is $G_{\text{eff}} = \left(\sqrt{G} + \sqrt{G-1} \right)^2$.

2.3.2 Modulation Transfer Function and Simulated Imagery

The Harris team supplemented its hypothesis-testing resolution analysis with image simulations based on our understanding of the modulation-transfer function (MTF) and noise spectral density of the baseline and quantum-enhanced sensors. For these simulations we modified the assumed setup to include 50/50 beam splitting *prior* to a pair of identical soft-aperture homodyne receivers that are arranged to measure the real and imaginary quadratures, respectively.[7] Coherent combining of their outputs then yields the following complex-valued baseband random process after matched filtering for the transmitter's pulse shape:[8]

$$y(\vec{\rho}) = \sqrt{\eta G_{\text{eff}}} \int \sqrt{E_T} \left(\frac{\sqrt{\pi R^2}}{2\lambda L} \right) \xi_T(\vec{\rho}')\xi_P(\vec{\rho}-\vec{\rho}')T(\vec{\rho}')d\vec{\rho}' + n(\vec{\rho}), \qquad (14)$$

where $n(\vec{\rho})$ is a zero-mean, complex-valued, isotropic Gaussian noise process with spectral density

$$S_{nn}(\vec{f}) = \eta G_{\text{eff}} \left(|P(\lambda L \vec{f})|^2 + (1-|P(\lambda L f)|^2)e^{-r} \right) + \left(1-\eta\right). \qquad (15)$$

For a speckle target we have that $T(\vec{\rho})$ can be taken to be a zero-mean, complex-valued, isotropic Gaussian random process with correlation function

$$\left\langle T(\vec{\rho_1}')T^*(\vec{\rho_2}') \right\rangle = \lambda^2 \mathcal{T}(\vec{\rho_1}')\delta(\vec{\rho_1}'-\vec{\rho_2}'), \qquad (16)$$

where the target's average intensity reflectivity, $\mathcal{T}(\vec{\rho_1}')$, is what the sensor is trying to image.

The physical content of the preceding analysis — and hence the core concept of our Type-2 quantum image enhancer — is illustrated in Figs. 7-9, where, for convenience, the figures have been drawn for a 1-D soft-aperture LADAR viewing a target yielding a baseband complex envelope at the receiver with spatial-frequency spectra $|S(f)|^2$ and $S_n(f)$ arising from its signal (image) and noise components, respectively.[9] Figure 7 shows a pictorial representation of how phase-sensitive amplification can recover the SNR that is lost because of sub-unity homodyne efficiency. Figure 8 shows how squeezed-vacuum injection can recover the SNR that is lost at high spatial frequencies

---

[7] The details of this configuration, the derivation of the modulation transfer results summarized below, and an extensive set of simulation results plus accompanying explanations appear in [11]-[13].

[8] Equations (14) and (15) are written for the SVI plus PSA system. The baseline sensor results are recovered by setting $G_{\text{eff}} = 1$ and $r = 0$, where the first condition turns off the PSA and the second turns off the SVI.

[9] The definitions of these signal and noise spectra — along with the normalization convention that is employed in Figures 7-9 — are given in [13].

because of the soft-aperture attenuation *if* the receiver has unity homodyne efficiency. Figure 8 also shows how SVI *loses* its effectiveness, in this regard, at low homodyne efficiency. Figure 9 shows how combining SVI with PSA can recover the SNR that is lost at high spatial frequencies because of the soft-aperture attenuation *despite* there being sub-unity homodyne efficiency. For additional details see [13].

Using this analysis we carried out MATLAB® simulations to establish the subjective imaging benefits afforded by SVI plus PSA when viewing a speckle-limited USAF test target pattern. Our simulations confirmed the resolution predictions found for the point-target hypothesis testing problem. Figure 10 depicts two 100-frame-averaged images (i.e., each image is averaged over 100 independent speckle shots) from simulations both taken at –3.3 dB single-frame SNR: the left is a baseline sensor image, and the right is a quantum sensor image with 15 dB SVI and 10 dB PSA gain showing a combined 10× resolution-cell improvement over the baseline sensor. The red boxes in Figure 10 highlight the smallest resolvable slit spacing in each case.
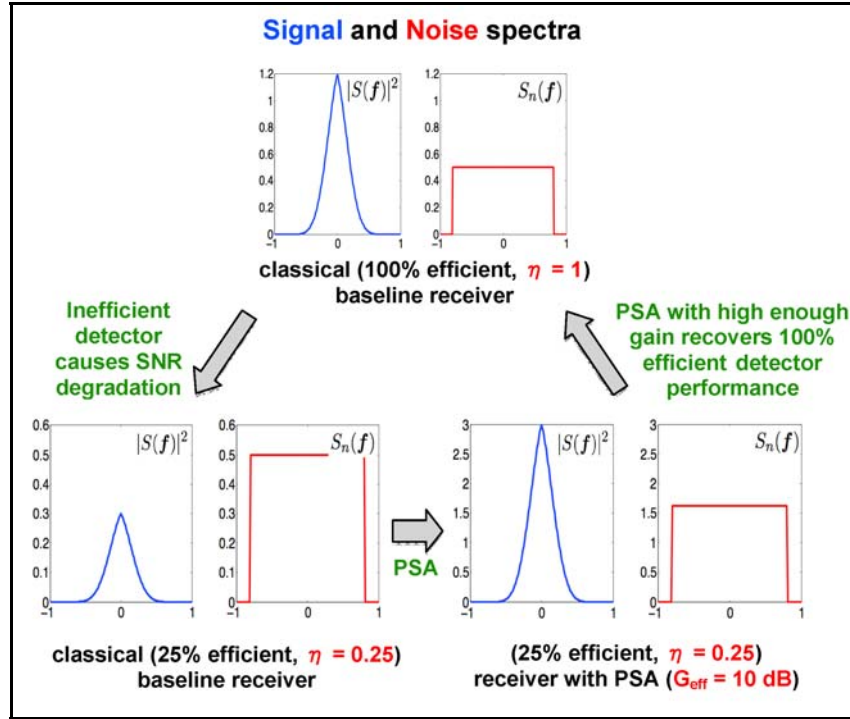
Figure 7: Pictorial representation of the value of PSA in compensating for low homodyne efficiency
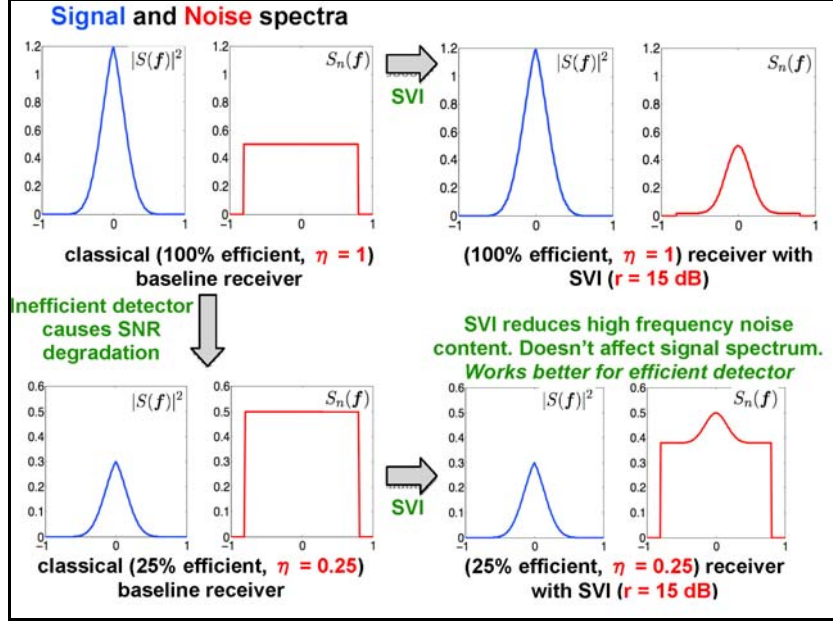
Figure 8: Pictorial representation of the value of SVI in compensating for the loss of high spatial frequency information caused by soft-aperture attenuation and the reduction in SVI effectiveness at low homodyne efficiency
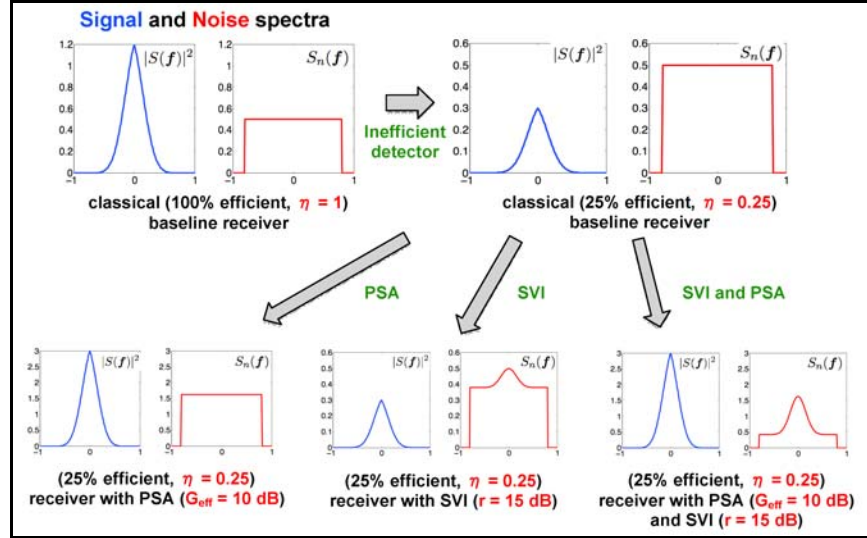
Figure 9: Pictorial representation of the value of SVI plus PSA in compensating for the loss of high spatial frequency information caused by soft-aperture attenuation in the presence of low homodyne efficiency.
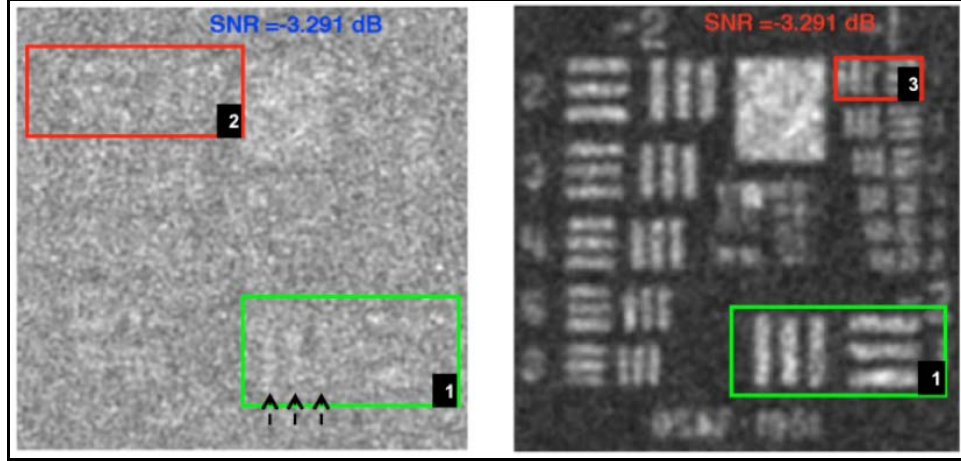
Figure 10: Simulated images of a USAF test pattern with the baseline sensor (left) and the SVI+PSA quantum sensor (right)

2.4 Quantum Illumination

The Harris team's work on quantum illumination — a Type-3 sensing system — stemmed from Lloyd's proof [14] that a large performance gain accrues from the use of entanglement in single-photon target detection within a lossy, noisy environment when compared to what can be achieved with unentangled single-photon states. The analysis in [14] was confined to a regime in which at most one photon arrives at the receiver from each LADAR transmission, regardless of whether the object of interest is absent or present. In order to understand whether or not quantum illumination could satisfy the requirements of the DARPA Quantum Sensors Program — or other sensing problems of DoD interest — Lloyd's work first had to be converted to a form that could account for arbitrary photon fluxes. In what follows we will summarize the results we have obtained, in this regard, which span target detection, angular resolution, and secure communication. We will also show how our quantum illumination systems avoid the Type-3 No-Go Theorem from Section 2.2 but may fall prey to a practical no-go condition.

2.4.1 Quantum Illumination for Improved Target Detection

Consider the following LADAR target-detection problem. The transmitter emits a pulse that interrogates a particular azimuth-elevation-range bin in which a target may, or may not, be present with equal probability for both hypotheses. Regardless of whether the target is present, the LADAR receiver will collect isotropic Gaussian noise originating from the interrogated bin. The LADAR's task is to make a minimum error probability decision as to whether the target is absent or present. In a conventional LADAR system, the transmitter emits a coherent-state pulse. In the quantum-illumination LADAR, the transmitter emits a T-sec-long pulse from the signal-port output of a continuous-wave (cw) spontaneous parametric downconversion (SPDC) source with W Hz phase-matching bandwidth, while retaining the accompanying idler pulse for use in conjunction with the light returned from azimuth-elevation-range bin under interrogation. In [15] we have reported exponentially-tight bounds on the error probabilities for optimum reception in the conventional and quantum-illumination LADARs. The essence of that analysis is summarized below.

Let $\left\{ \hat{a}_{S_m}, \hat{a}_{I_m} : 1 \leq m \leq M \right\}$ be the photon annihilation operators for the $M = W\,T$ signal-idler mode pairs that comprise the SPDC transmitter's output. These mode pairs are in independent identically distributed (iid), zero-mean, maximally-entangled Gaussian states with average photon number per mode $N_S \ll 1$. The return modes from the target bin will have photon annihilation operators $\left\{ \hat{a}_{R_m} : 1 \leq m \leq M \right\}$ given by $\hat{a}_{R_m} = \hat{a}_{B_m}$ when the target is absent (hypothesis H_0), and $\hat{a}_{R_m} = \sqrt{\kappa}\,\hat{a}_{S_m} + \sqrt{1-\kappa}\,\hat{a}_{B_m}$ when the target is present (hypothesis H_1). Here, $\kappa \ll 1$ is the transmitter-to-target-to-receiver coupling when the target is present, and the background-light modes, $\left\{ \hat{a}_{B_m} \right\}$, are in iid, zero-mean isotropic Gaussian states with average photon number N_B under hypothesis H_0 and $N_B /(1-\kappa)$ under hypothesis H_1.[10] Because the performance advantage of SPDC quantum illumination arises in scenarios that are *both* lossy *and* noisy, we shall assume that $N_B \gg 1$, even though this is *not* the case at LADAR wavelengths unless the system is being actively jammed.[11] The hypothesis-testing setup for the conventional LADAR system is identical to that of the quantum-illumination system with one exception: the transmitter emits signal modes $\left\{ \hat{a}_{S_m} : 1 \leq m \leq M \right\}$ that are in coherent states with average photon number per mode $N_S \ll 1$.

---

[10] These choices for the background light's average photon number under the two hypotheses preclude the presence of a passive signature in the light collected from the chosen azimuth-elevation-range bin.

[11] Our $N_B \gg 1$ assumption will be satisfied, however, in the microwave region.

In this lossy ($\kappa \ll 1$), noisy ($N_B \gg 1$), low-brightness ($N_S \ll 1$) regime we have obtained the following bounds on the error probabilities achieved by the quantum-illumination (*QI*) and coherent-state (*CS*) LADARs:

$$\Pr(e)_{QI} \leq \frac{\exp\left(-M\kappa N_S / N_B\right)}{2} \tag{17}$$

$$\Pr(e)_{CS} \leq \frac{\exp\left(-M\kappa N_S / 4N_B\right)}{2}. \tag{18}$$

The coherent-state bound is a Chernoff bound, and is therefore exponentially tight, i.e.,

$$\lim_{M \to \infty}\left[-\ln\left[2\Pr(e)_{CS}\right]/M\right] = \kappa N_S / 4N_B, \tag{19}$$

whereas the quantum-illumination bound is a weaker Bhattacharyya bound. Comparison of Eqs. (17) and (18) suggests that the quantum-illumination LADAR can achieve the same performance as the coherent-state LADAR with 6 dB (factor-of-four) fewer photons. Further support for the advantageous behavior of quantum illumination derives from the *lower* bound

$$\Pr(e)_{CS} \geq \frac{\exp\left(-M\kappa N_S / 2N_B\right)}{4}, \tag{20}$$

which applies in the lossy, noisy, low-brightness regime when $M\kappa N_S / 2N_B \gg 1$. This result shows that quantum illumination is *at least* 3 dB superior, in error exponent, to the coherent-state LADAR. Moreover, as shown in [15], Eq. (20) bounds the performance of all classical-state LADARs in this operating regime.

The preceding performance results presume that optimum quantum receivers are used by both the coherent-state and quantum-illumination LADARs. Homodyne reception has been shown to be a good approximation to the optimum quantum receiver for the coherent-state LADAR in the lossy, noisy operating regime we are considering, but no explicit implementation has been found, as yet, for the quantum-illumination LADAR's optimum quantum receiver. We have shown [16], however, that an optical parametric amplifier (OPA) can be used to implement a receiver that can achieve

$$\Pr(e)_{OPA} \leq \frac{\exp\left(-M\kappa N_S / 2N_B\right)}{2} \tag{21}$$

when $\kappa \ll 1$, $N_B \gg 1$, and $N_S \ll 1$, which is an error exponent that is 3 dB better than that of the coherent-state LADAR's Chernoff bound, thus closing half the performance gap between the optimum quantum receiver for the coherent-state LADAR and the

optimum quantum receiver for the QI LADAR. The OPA receiver works by applying the return mode and idler mode to the OPA's idler and signal input ports, respectively, and performing photon counting on the OPA's signal-port output. By tuning the OPA gain to its optimal value, which turns out to be near unity, we obtain the error bound in Eq. (21). An explicit comparison of our error probability results — obtained without assuming the asymptotic $\kappa \ll 1$, $N_B \gg 1$, and $N_S \ll 1$ conditions — is presented in Figure 11; see [16] for more details. The blue-shaded region in Figure 11 lies between the Chernoff upper bound and the lower bound on error probability of the coherent-state LADAR's optimum receiver, with the lower bound also applying to any classical-state LADAR. The pink shaded region lies between the Bhattacharyya upper bound and the lower bound on the error probability of the quantum-illumination LADAR's optimum receiver. Also shown are the error probability for a coherent-state LADAR that uses homodyne reception, and that for a quantum-illumination LADAR that uses an optical parametric amplifier (OPA) receiver. All the results assume that $\kappa = 0.01$, $N_S = 0.01$, and $N_B = 20$. Here we see that there is a definite region in which the quantum-illumination LADAR's optimum receiver has an error probability that is substantially lower than that of any classical-state LADAR. Moreover, Figure 11 shows that quantum illumination with OPA reception outperforms coherent-state operation with homodyne reception, which is known to approximate the optimum quantum receiver for this LADAR in the lossy, noisy operating regime. Note that the target-detection performance advantage we have found for quantum-illumination LADAR, as compared to classical-state systems of the same average transmitted photon number, does not conflict with the Type-3 No-Go Theorem we stated in Section 2.2 because that theorem does not encompass the low-brightness ($N_S \ll 1$) high mode-number ($M \gg 1$) region of interest for quantum illumination. Indeed, the Bhattacharyya bound for the quantum-illumination LADAR in the lossy, noisy regime with a high-brightness ($N_S \gg 1$) source, has the *same* error exponent as the coherent-state LADAR of the same average transmitted photon number.
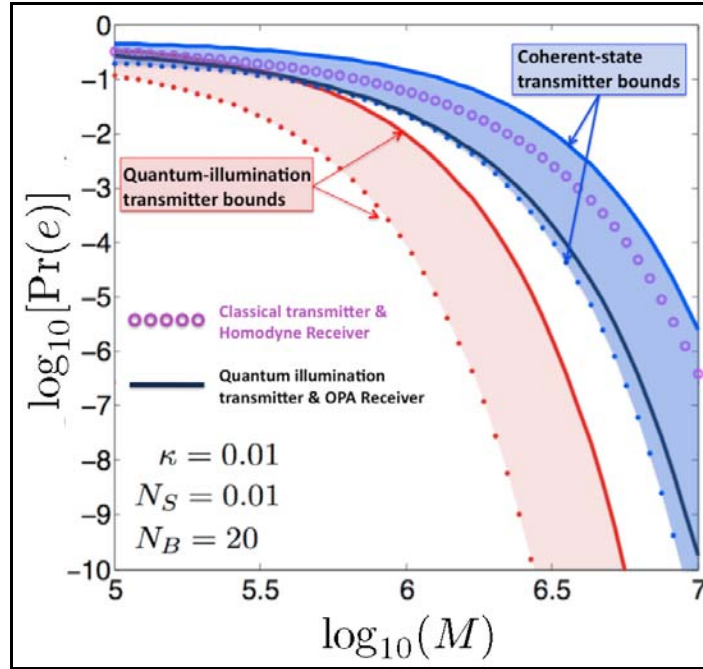
Figure 11: Target-detection performance comparison between coherent-state and quantum-illumination LADARs

2.4.2 Quantum Illumination for Improved Angular Resolution

Paralleling the development of one-versus-two target angular resolution that we performed for its SVI plus PSA Type-2 LADAR, the Harris team extended the comparison between quantum-illumination and conventional LADAR systems to this angular resolution scenario. The two equally-likely hypotheses are H_1, the LADAR return comes from an on-axis specular point target, and H_2, the LADAR return comes from a pair of equal strength, in-phase specular point targets that are symmetrically disposed about the optical axis. Under both hypotheses the channel is very lossy, i.e., the transmitter-to-target-to-receiver coupling coefficient satisfies $\kappa \ll 1$. The channel is also very noisy, viz., in addition to their target reflections, the received modes contain iid zero-mean isotropic Gaussian noise with average photon number $N_B \gg 1$. The full characterization of this hypothesis test appears in [17], with a calculation approach — for finding the Chernoff bounds on the error probabilities of coherent-state and quantum-illumination LADARs — that employs the symplectic decomposition technique described in [15] for the target-detection case. So far, however, we have been unable to develop analytic results for the Chernoff-bound error exponents of either LADAR. Nevertheless, our numerical evaluations indicate that, as in the case of target detection, a substantial reduction in error probability is obtained from a quantum-illumination system that uses the same average transmitted photon number as its coherent-state counterpart. Figure 12 shows an example of this performance advantage by plotting the Chernoff bounds versus the number of mode pairs, M, that are employed. In Figure 12 the one-target hypothesis is an on-axis specular point target. The two-target hypothesis is a pair of equal-strength, specular point targets that are at angles $\pm\theta$ with respect to the optical axis that together return the same average photon number as the single target. All the results are quantum Chernoff bounds that assume $\kappa = 0.01$, $N_S = 0.01$, $N_B = 20$, and a hard-aperture receiver entrance pupil of diameter D.

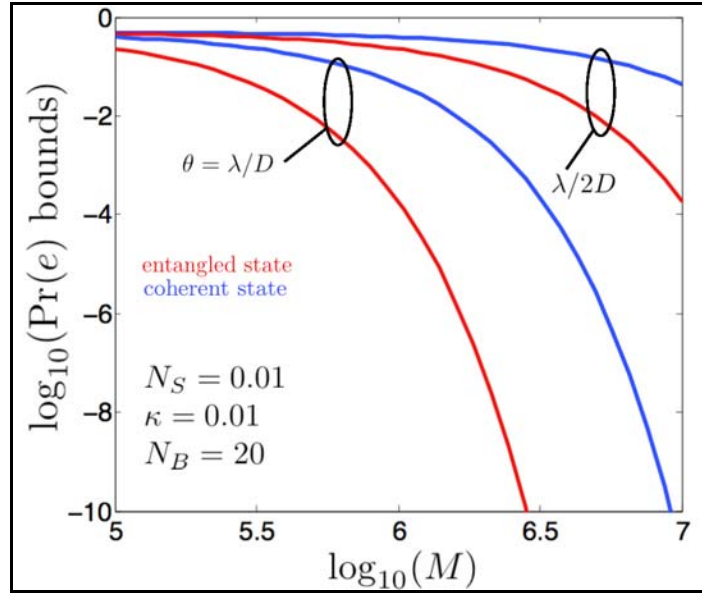**Figure 12: One-versus-two target discrimination performance comparison between coherent-state (blue curves) and quantum-illumination (red curves) LADARs**

Three additional points are worth noting at this juncture. First, the error probability advantage afforded by quantum illumination will translate into an improvement in angular resolution, as illustrated in Figure 13 for a different choice of system and propagation parameters. Here we have lowered the average photon number of the background from the value used in Figure 12, although N_B is still much larger than what will prevail — in the absence of jamming — at LADAR wavelengths. In Figure 13 the results are plotted versus the average received photon number that is due to the target (or targets) divided by the average received photon number from the background. There is a $1.5\times$ enhancement in angular resolution when $\kappa N_S / N_B$ = -32 dB. We have also chosen a range of values for N_S that extends beyond the low-brightness regime. This choice was made partly to reduce the required mode number M — and hence the pulse duration for a given SPDC phase-matching bandwidth — and partly to illustrate quantum-illumination's loss of performance advantage in the high-brightness regime. Second, we again avoid the Type-3 No-Go Theorem from Section 2.2 because Figs. 12 and 13 employ $M\gg1$ mode pairs. Finally, unlike our SVI plus PSA Type-2 sensor, the quantum illumination system considered here obtains its resolution improvement with a hard-aperture pupil. Of course, we have not shown that quantum illumination can cope with the 100 dB loss that may be present in the Figure 1 LADAR scenario, nor have we evaluated its resolution improvement for targets that produce fully-developed speckle returns. Nevertheless, there may be some scenarios in which quantum illumination imaging sensors could provide useful performance improvements over conventional systems, when compared at equal average transmitted photon number. However, as we shall discuss in Section 2.4.4, any enthusiasm for that possibility must be tempered by the practical no-go conditions that we have identified in our Phase I work.
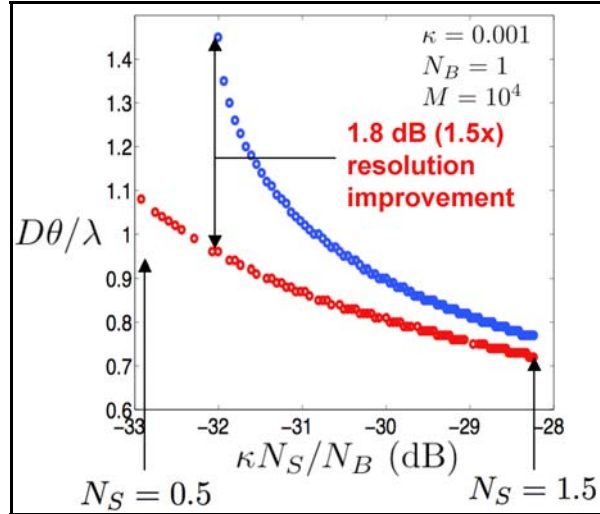
Figure 13: Angular resolution θ, defined by Pr(e)= 0.03 one-versus-two target discrimination error probability and normalized by the diffraction scale λ/D

2.4.3 Quantum Illumination for Secure Communication

The remarkable feature about the quantum illumination results we have presented in Sections 2.4.1 and 2.4.2 is that significant performance advantages accrue from the use of an entangled-state source despite the fact that the channel — from the transmitter to the target and back to the receiver — destroys this entanglement. Indeed, consider the case of quantum-illumination target detection. The signal-idler mode pairs produced by SPDC are in iid, zero-mean, jointly Gaussian states with the common Wigner-distribution covariance matrix

$$\Lambda_{SI} = \frac{1}{4} \begin{bmatrix} 2N_S + 1 & 0 & 2\sqrt{N_S(N_S+1)} & 0 \\ 0 & 2N_S + 1 & 0 & -2\sqrt{N_S(N_S+1)} \\ 2\sqrt{N_S(N_S+1)} & 0 & 2N_S + 1 & 0 \\ 0 & -2\sqrt{N_S(N_S+1)} & 0 & 2N_S + 1 \end{bmatrix}. \quad (22)$$

When the target is present (hypothesis H_1), the return-idler mode pairs are also in iid, zero-mean, jointly Gaussian states[12] whose common Wigner-distribution covariance matrix is now given by

$$\Lambda_{RI} = \frac{1}{4} \begin{bmatrix} 2\kappa N_S + 2N_B + 1 & 0 & 2\sqrt{\kappa N_S(N_S+1)} & 0 \\ 0 & 2\kappa N_S + 2N_B + 1 & 0 & -2\sqrt{\kappa N_S(N_S+1)} \\ 2\sqrt{\kappa N_S(N_S+1)} & 0 & 2N_S + 1 & 0 \\ 0 & -2\sqrt{\kappa N_S(N_S+1)} & 0 & 2N_S + 1 \end{bmatrix}. \quad (23)$$

---

[12] Gaussian states retain their Gaussian character under linear transformations, and our transmitter-to-target-to-receiver transformation is linear, with inputs — the signal-idler mode pairs and the background light — that are in Gaussian states.

The non-zero off-diagonal terms in Eqs. (22) and (23) represent phase-sensitive cross correlations, while the vanishing of the other off-diagonal elements indicates that these states have no phase-insensitive cross correlations. It is known that the strength of such phase-sensitive cross correlations is limited by the values of the diagonal entries in the Wigner-covariance matrix. Thus, Eq. (22) is a maximally-entangled state because it saturates the quantum-mechanical upper limit, $\sqrt{N_S(N_S+1)}/2$, on the magnitude of the phase-sensitive cross correlations. Moreover, in the low-brightness regime, wherein $N_S \ll 1$ prevails, the magnitudes of these phase-sensitive cross correlations greatly exceed their classical upper limit $N_S/2$. On the other hand, when $N_B \geq \kappa$ holds, the magnitudes of the phase-sensitive cross correlations in Eq. (23) lie at or below the classical-state upper limit. Then, because these are Gaussian states, it turns out that they are classical and hence *cannot* be entangled.[13]

It is now possible to see why quantum illumination works in a lossy, noisy, entanglement-destroying environment when the SPDC source operates at low brightness. If $N_S \ll 1$, then the magnitude of the ensuing phase-sensitive cross correlations between the target return and the idler, although within classical-state limits, greatly exceeds what any classical source is capable of producing, viz., the former will be approximately $\sqrt{\kappa N_S}/2$, whereas the maximum the latter can provide is the much smaller $\sqrt{\kappa} N_S/2$.

Having understood this underlying explanation for the benefits of quantum illumination, we have used that knowledge to conceive a new protocol for secure communication in the presence of passive eavesdropping. The basic construct is shown in Figure 14 where the relevant annihilation operators are shown on each propagation path. Full details appear in [18],[19], so we shall content ourselves here with a brief description of the system, its performance, and related future avenues for research.

---

[13] Physically, adding iid, zero-mean, isotropic Gaussian noise of average photon number N_B/κ to the signal mode at the SPDC source will produce the output state characterized by Eq. (23) when there is no additional background injected by the channel. Thus what we have is a signal-idler classicalization that only needs to add at least one noise photon per signal mode to classicalize the maximally-entangled state, cf. the Classicalization Theorem and the Type-3 No-Go Theorems from Section 2.2.
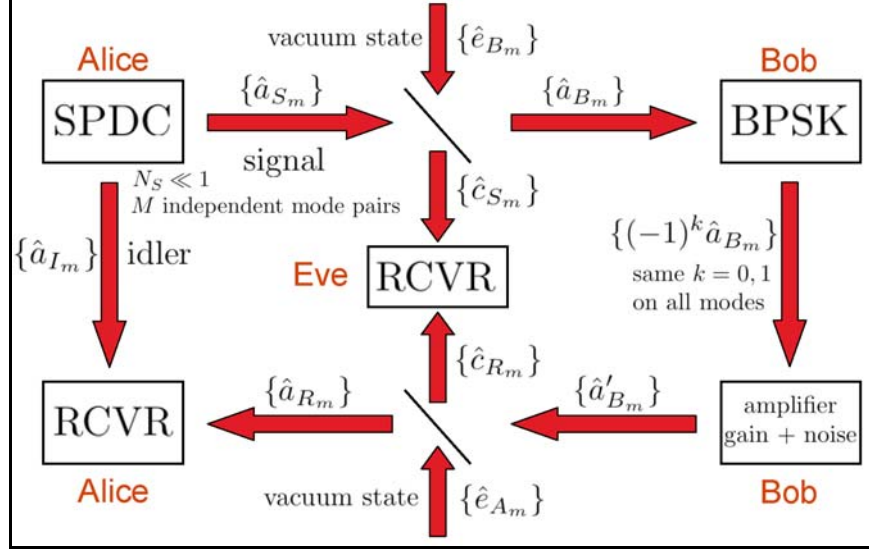
Figure 14: Configuration for defeating passive eavesdropping via quantum illumination

As in the quantum illumination LADARs considered in previous subsections, Alice's SPDC source in Figure 14 produces a *T*-sec-long pulse comprising $M = WT$ iid, zero-mean, maximally-entangled, signal-idler mode pairs. She sends her signal modes to Bob, through a pure-loss channel of transmissivity κ in which the eavesdropper (Eve) collects all the light that does not reach him, while retaining her idler modes for future use. Bob imposes binary phase-shifted keyed (BPSK) modulation on his received signal pulse, passes it through a phase-insensitive amplifier — with gain *G* and output-noise average photon number $N_B + 1$— and sends the resulting light back to Alice through the same transmissivity-κ pure-loss channel. Eve gets all the light sent by Bob that does not reach Alice.

We have derived the Chernoff bounds for the error probabilities of Alice and Eve's optimum quantum receivers, along with a lower bound on the error probability of Eve's optimum quantum receiver and the Bhattacharyya bound on Alice's OPA receiver. In the lossy ($\kappa \ll 1$), low-brightness ($N_S \ll 1$), high-noise ($\kappa N_B \gg 1$) regime we have found the following simple asymptotic forms for these error probability bounds:

$$\Pr(e)_{\text{Alice}} \leq \frac{\exp(-4M\kappa GN_S / N_B)}{2} \tag{24}$$

$$\Pr(e)_{\text{Eve}} \leq \frac{\exp(-4M\kappa(1-\kappa)GN_S^2 / N_B)}{2} \tag{25}$$

$$\Pr(e)_{\text{Eve}} \geq \frac{1-\sqrt{1-\exp(-8M\kappa(1-\kappa)GN_S^2 / N_B)}}{2} \tag{26}$$

$$\Pr(e)_{\text{OPA}} \le \frac{\exp(-2M\kappa GN_S/N_B)}{2}. \tag{27}$$

These results show that despite Eve's receiving the lion's share of the photons sent by Alice to Bob and by Bob to Alice, the Chernoff bound error exponent on her optimum quantum receiver will be substantially inferior to the Bhattacharyya bound error exponent of Alice's OPA receiver because $2N_S/(1-\kappa) \ll 1$. An explicit example of our error probability bounds — calculated numerically for the case $N_S = 0.004$, $\kappa = 0.1$, $G = N_B = 10^4$ without using the asymptotic approximations employed in deriving Eqs. (24)-(27) — is shown in Figure 15. Solid curves in Figure 15 are Chernoff upper bounds on Alice and Eve's optimum quantum receivers. Dashed curve is the lower bound on Eve's optimum quantum receiver. Dot-dashed curve is the Bhattacharyya bound on Alice's optical parametric amplifier (OPA) receiver.
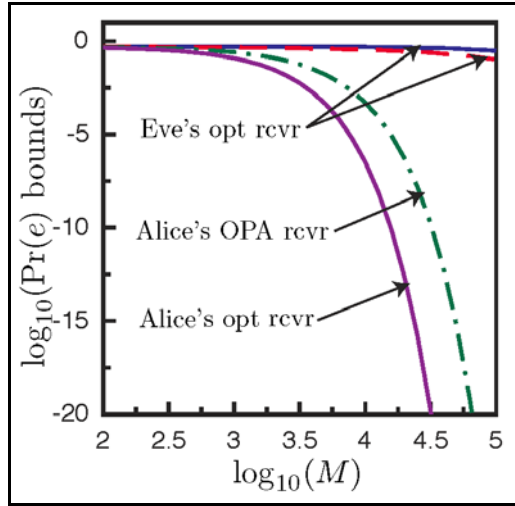
Figure 15: Error probability bounds for $\kappa = 0.1$, $N_S = 0.004$, $G = N_B = 10^4$ plotted versus the number of SPDC mode pairs

Several final points are worth noting in conjunction with this communication scheme. First, it is a phase-sensitive system, so Alice's receiver will require phase coherence that must be established through a tracking system. Second, there is a path-length versus bit-rate tradeoff. Operation must occur in the low-brightness regime. So as the channel's transmissivity decreases, Alice must increase her mode-pair number M to maintain the same error probability at a fixed N_S value. With $W = 1$ THz, and $T = 20$ ns, so that $M = WT = 2 \times 10^4$, the case shown in Figure 15 will yield 50 Mbit/s communications with $\Pr(e)_{\text{OPA}} \le 5.09 \times 10^{-7}$ and $0.285 \le \Pr(e)_{\text{Eve}} \le 0.451$ when Alice and Bob are linked by 50 km of 0.2 dB/km loss optical fiber and the rest of their equipment is ideal. Although this example indicates that Alice and Bob enjoy tremendous immunity to a *passive* Eve, to make the Figure 14 system *unconditionally* secure Alice and Bob must take steps to

defeat Eve's use of impersonation attacks, man-in-the-middle attacks, and optical probing of Bob's BPSK modulator. We believe that these attacks can be identified and dealt with if Alice and Bob employ authentication, monitor the physical integrity of the communication channel, check the received power level and its frequency spectrum at Bob's station, and verify the error probability at Alice's station. Substantiating that belief will be the subject of future research.

2.4.4 Practical No-Go Conditions for Quantum Illumination

The Type-3 No-Go Theorem from Section 2.2 is not in conflict with the quantum-illumination performance improvements that we have found in the low-brightness, high mode-pair number regime because this theorem does not apply there. While we are still working on fundamental go/no-go results for more general cases than those treated by that theorem, it is important to note that *practical* considerations may make quantum illumination less attractive as a route to enhanced imaging. Such practical no-go conditions are developed at some length in [5]. Here we shall limit our discussion to the most significant of those conditions, which follows immediately from the Classicalization and Quantum Measurement-Bound Theorems presented in Section 2.2.

Sections 2.4.1 and 2.4.2 show that Type-3 sensing with an SPDC source can improve target detection and angular resolution performance when a quantum-illumination LADAR is compared with a coherent-state LADAR that interrogates the target region with a transmitter beam of the same average photon number. The Classicalization Theorem implies that essentially the same detection and angular resolution performance as the quantum illumination LADAR can be obtained by using the classical signal-idler transmitter state obtained by adding iid, zero-mean, isotropic Gaussian noise of unity average photon number to every signal and idler mode. For an M mode-pair system, this means that we have a classical-state system, with average transmitted (signal) photon number $M(N_S + 1)$ per pulse, whose performance matches that of the quantum-illumination LADAR whose average transmitted photon number per pulse is MN_S. Of course, the former is much higher than the latter, because we are working at low brightness, i.e., $N_S \ll 1$. However, for quasimonochromatic operation, the additional power required by this classical-state source, $W\hbar\omega$ at center frequency ω, is a trivial amount, e.g., 0.13 μW for a 1THz phase-matching bandwidth at $\lambda = 1.55 \mu$m wavelength. It follows that our interest in quantum illumination for imaging applications may need to focus on scenarios — such as those involving low probability of detection, low-probability of interception — in which transmitting the absolute minimum amount of power is essential.

2.5 Ghost Imaging

Ghost imaging is the acquisition of object information by means of photocurrent correlation measurements. Its first demonstration utilized a biphoton source, thus the image was interpreted as a quantum phenomenon owing to the entanglement of the source photons. Subsequent experimental and theoretical work demonstrated that ghost imaging could be performed with pseudothermal light, i.e., cw laser light that had been

transmitted through a rotating ground-glass diffuser. Whereas the biphoton requires a quantum description for its photodetection statistics, pseudothermal light is in a classical state whose photodetection statistics can be treated via the semiclassical (shot-noise) theory of photodetection. This disparity has sparked interest in the physics of ghost imaging. Recently [2], we established a Gaussian-state analysis of ghost imaging that unified prior work on biphoton and pseudothermal sources. Our analysis indicated that ghost-image formation is intrinsically due to classical coherence propagation, with the principal advantage afforded by the biphoton state being high-contrast imagery in the wideband limit. Other recent work [20],[21], however, has offered an alternative explanation for pseudothermal-light ghost imaging: nonlocal two-photon quantum interference. In Section 2.5.1, we will summarize our findings [22] with respect to the signal-to-noise ratios (SNRs) of biphoton and pseudothermal ghost imaging. In Section 2.5.2 we will summarize our theoretical demonstration [23] that ghost imaging can be accomplished with only *one* detector, viz., the bucket detector that collects a single pixel of light which has interacted with the object. As only one light beam and one photodetector are required, this imaging configuration cannot depend on nonlocal two-photon interference. Moreover, it affords background-free imagery in the narrowband limit plus a 3-D sectioning capability, and these characteristics have been demonstrated in a recent experiment [24]. In Section 2.5.3 we return to the pseudothermal ghost imager, and discuss its prospects for achieving high-resolution imagery in the presence of atmospheric turbulence.

2.5.1 Gaussian-State SNR Analysis for Biphoton and Pseudothermal Ghost Imaging

In the absence of pump depletion, continuous-wave SPDC produces signal and idler beams that are in a maximally-entangled, zero-mean, jointly Gaussian state with zero phase-insensitive cross correlation and maximum phase-sensitive cross correlation. In the low-brightness limit, with photon flux low enough that at most one signal-idler photon pair is present within a photodetection measurement interval, this jointly Gaussian state reduces to a predominant vacuum state plus a weak biphoton component. Likewise, 50/50 beam splitting of pseudothermal light, as is done in pseudothermal ghost imaging, results in a pair of light beams that are in a classical, zero-mean jointly Gaussian state with a maximum phase-insensitive cross correlation and no phase-sensitive cross correlation.

Figures 16 and 17, respectively, show the configurations for lensless biphoton and pseudothermal ghost imaging of a transmission mask. In both cases these setups produce ghost images because the light beam that has interacted with the transmission mask is collected by a single-pixel (bucket) photodetector that affords no spatial resolution, whereas the scanning pinhole detector — alternatively a CCD camera — provides spatial resolution on the light beam it detects but that light beam has not interacted with the object. Nevertheless, when the outputs from these two detectors are correlated — or, at sufficiently low light levels, photon coincidence counting is performed — the resulting correlation (or coincidence) pattern, $C(\rho_1)$, contains an image of the mask's intensity transmission $|T(\rho)|^2$.
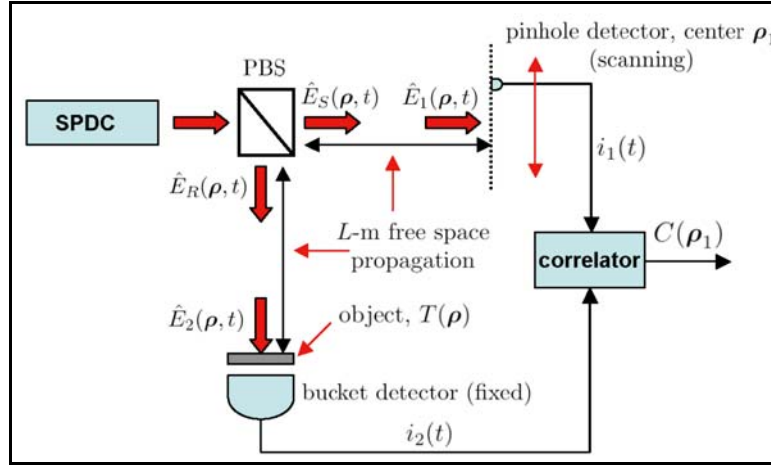

Figure 16: Configuration for biphoton ghost imaging of a transmission mask. PBS denotes polarizing beam splitter
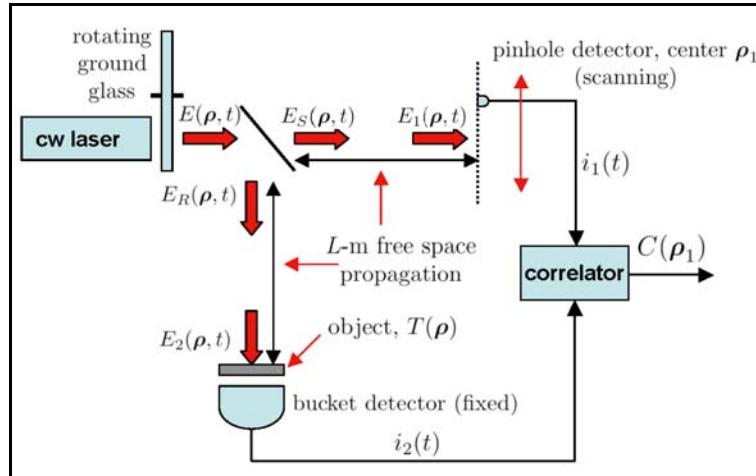

Figure 17: Configuration for pseudothermal ghost imaging of a transmission mask

35

Previously [2] we used Gaussian-state analysis to determine the spatial resolution and field-of-view characteristics of both biphoton and pseudothermal ghost imaging by evaluating the ensemble average $\langle C(\rho_1) \rangle$. There we considered both their respective near-field and far-field regions, i.e., when the measurement-plane cross correlations were approximately equal to their source-plane counterparts (near-field operation) and when those measurement-plane correlations were appropriate Fourier transforms of the source-plane correlations. In all cases we found that classical coherence propagation accounted for ghost image formation, with the very strong non-classical phase-sensitive cross correlation of the biphoton limit being responsible for the virtual absence of a background term in its resulting ghost image. However, this prior work did not include an SNR analysis that would permit determination of the averaging time needed to ensure that a time-average correlation measurement gave a high-fidelity replica of $\langle C(\rho_1) \rangle$. This task was accomplished during our Phase I Quantum Sensors Program. Our complete results have been published [22], so we will merely illustrate their content here with Figures 18 and 19. The former plots the far-field ghost imaging SNR behavior obtained using the maximally-entangled Gaussian-state SPDC source, while the latter shows corresponding behavior for the pseudothermal Gaussian-state source. The abscissa, in both figures, is the source brightness at the measurement planes, i.e., the average number of photons per spatiotemporal mode. It is given by $PT_0\rho_L^2/a_L^2$, where: P is the photon flux of the signal and reference beams in Figs. 16 and 17; T_0 is the source coherence time; $\rho_L = \lambda L/\pi a_0$ and $a_L = \lambda L/\pi \rho_0$ with a_0 and $\rho_0 \ll a_0$ being the source-plane intensity radius and coherence radius of the illumination. The other parameters entering into these figures are: T_I, the integration time used in time averaging the photocurrent cross correlations in Figs. 16 and 17; and Ω_B, the baseband bandwidth of the photodetectors. The solid curves in Figure 18 are exact results for three choices of the normalized source coherence time. The dashed and dot-dashed curves give the high-brightness and low-brightness asymptotes, respectively. Far-field propagation with a broadband ($\Omega_B T_0 \ll 1$) source is assumed. In Figure 19 the solid curves are exact results for three choices of the normalized source coherence time. The dashed and dot-dashed curves give the high-brightness and low-brightness asymptotes. Far-field propagation with a narrowband ($\Omega_B T_0 \gg 1$) source is assumed.

Figure 18: Normalized SNR versus measurement-plane source brightness for ghost imaging with a maximally-entangled Gaussian-state SPDC source

For the SPDC source we have chosen to display the broadband results, i.e., when the photodetector's baseband bandwidth Ω_B is much smaller than the source bandwidth $1/T_0$, whereas for the pseudothermal source we have chosen to plot the narrowband results, wherein $\Omega_B T_0 \gg 1$. These conditions represent typical operating regimes for the two sources.[14] In both cases we find that the SNR increases linearly with source brightness when brightness is sufficiently low, and saturates at a value that is independent of source brightness when brightness grows without bound. The SPDC SNR, however, overshoots its high-brightness asymptote, while the pseudothermal SNR never does. Interestingly, it turns out that the acquisition time needed for the broadband SPDC source to achieve a desired ghost-image SNR may be greater or less than the acquisition time needed for the narrowband pseudothermal source to achieve that same ghost-image SNR, depending on the values of the system parameters [22].

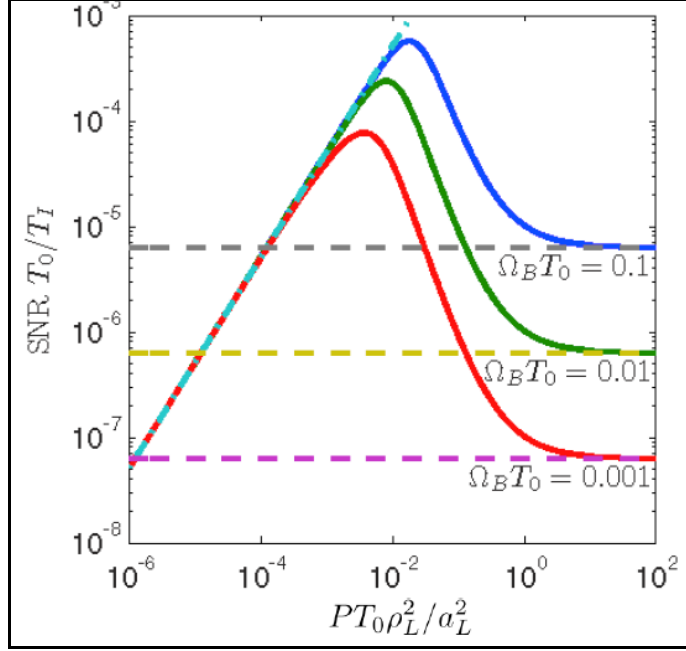[14] Results for the narrowband SPDC case and the broadband pseudothermal case appear in [22].
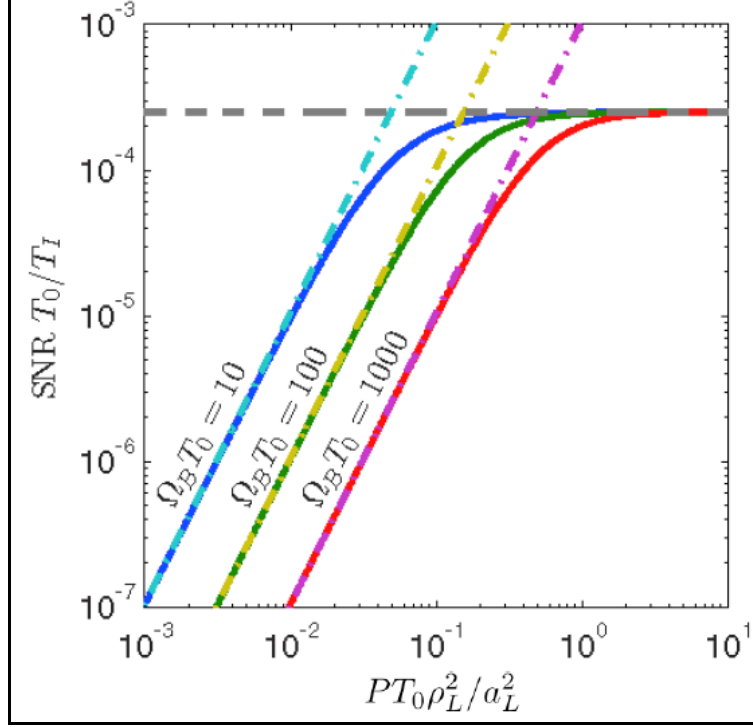
Figure 19: Normalized SNR versus measurement-plane source brightness for ghost imaging with a maximally-correlated Gaussian-state pseudothermal source

2.5.2   Computational Ghost Imaging

Having developed the Gaussian-state theory of pseudothermal ghost-image formation, it becomes a simple matter to identify two new configurations for lensless ghost imaging. First, rather than use cw laser light transmitted through a rotating ground glass as the source of a narrowband, spatially-incoherent light for ghost imaging, we can employ the configuration shown in Figure 20. Here, we transmit a cw laser beam through a spatial light modulator (SLM) whose inputs are chosen to create the desired coherence behavior. Specifically, we assume an idealized SLM consisting of $d \times d$ pixels arranged in a $(2K+1) \times (2K+1)$ array with 100% fill factor within a $D \times D$ opaque pupil, where $D = (2K+1)d$ and $K \gg 1$. We use this SLM to impose iid random phases on the light transmitted through each pixel with coherence time T_0 that is long compared to the response times of the photodetectors, $1/\Omega_B$. In this source's far field, we can expect to obtain ghost imagery with field-of-view and spatial-resolution characteristics approximating those of the pseudothermal imager with $\rho_0 \approx d$ and $a_0 \approx D$.

38

To realize the Figure 20 ghost imager we could use noise generators to drive the SLM, but it is more interesting to suppose that deterministic driving functions are employed. What we want at the SLM's output is a narrowband, zero-mean field whose spatial coherence — inferred now from a time average, rather than an ensemble average, because there is no true randomness — is limited to field points within a single pixel. Strong sinusoidal modulation, with different frequencies for each pixel, will work. This deterministically-modulated source will also yield a ghost image of spatial resolution comparable to that obtained using the pseudothermal source.
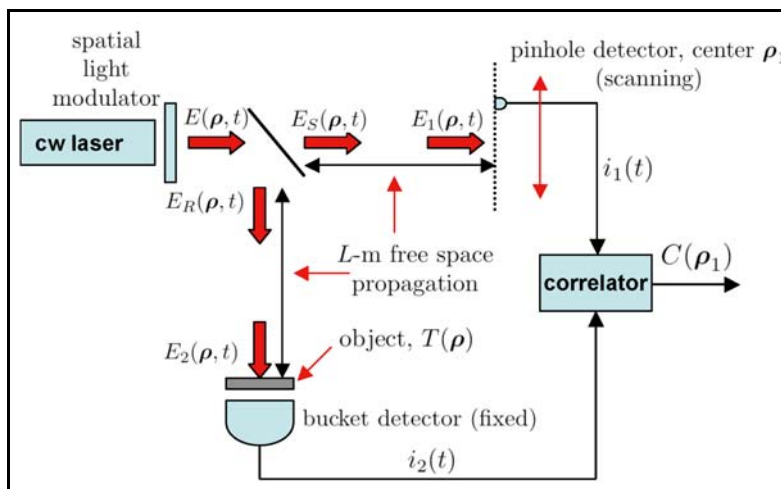
Figure 20: Configuration for spatial light modulator (SLM) ghost imaging of a transmission mask

At this point, the notion of computational ghost imaging — in which we only use the bucket detector — is easily understood, see Figure 21. We use deterministic modulation of a cw laser beam to create the field that illuminates the object transparency, and, as usual, we collect the light that is transmitted through the transparency with a bucket (single-pixel) detector. Knowing the deterministic modulation applied to the original cw laser beam allows us to use diffraction theory to *compute* the intensity pattern that would have illuminated the pinhole detector in the usual lensless ghost-imaging configuration. Furthermore, we can subtract the time average of this intensity, in our computation, and obtain the equivalent of the zero-mean intensity variation. To distinguish these computed values from actual light-field quantities, we put tildes on them. The time average correlation function, $\Delta \tilde{C}(\rho_1)$, will then be a background-free ghost image with spatial resolution and spatial extent akin to what would be obtained from pseudothermal ghost imaging with $\rho_0 \approx d$ and $a_0 \approx D$, and a DC block applied to the pinhole detector. Now, because only one photodetector has been employed, it is impossible to interpret this computational ghost image as arising from nonlocal two-photon interference.

In addition to obviating the need for a high spatial-resolution detector in ghost-image formation, at the expense of the computational burden associated with the free-space propagation calculation for the reference-arm field, computational ghost imaging permits 3-D sectioning to be performed. To see that this is so, we return to the pseudothermal ghost-imaging configuration from Figure 17 and evaluate its depth of focus, i.e., the ΔL value at which the ghost image becomes significantly blurred when the object is at $z = L$ but the pinhole detector is at $z = L + \Delta L$. This turns out to be $|\Delta L| = 2\lambda L^2/\pi a_0^2$, which, in the near-field of the pre-diffuser laser beam, is a very small fraction of the source-to-object path. This limited depth of focus has the following implications when a range-spread opaque object is imaged in reflection. The pseudothermal ghost imager can only image one focal region at a time. However, because the computational ghost imager can precompute $\Delta \tilde{I}_1(\rho_1, t)$ for a wide range of propagation distances, the same bucket-detector photocurrent can be correlated with many such $\Delta \tilde{I}_1(\rho_1, t)$ to perform 3-D sectioning of the object's reflectance. Of course, this sectioning further increases the computational burden, but this burden can be handled off-line, and, for a given SLM and its associated modulation waveforms, the *same* precomputed $\Delta \tilde{I}_1(\rho_1, t)$ can be used for *all* ghost images formed using that system.
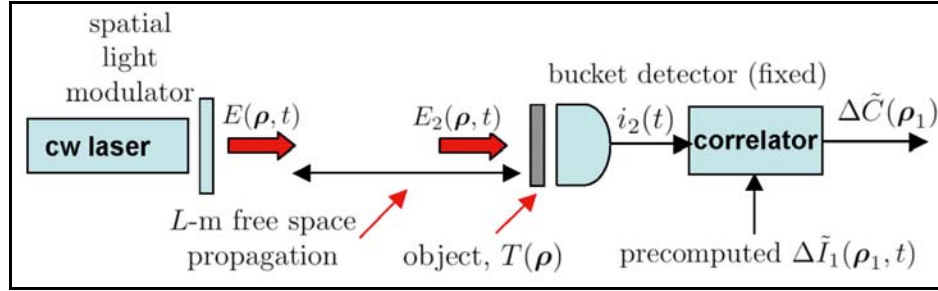

Figure 21: Configuration for computational ghost imaging of a transmission mask

More information about the theory of computational ghost imaging appeared in [23], with initial experimental confirmation — by the Y. Silberberg group from the Weizmann Institute — being presented in [24].

2.5.3 Potential for Achieving Turbulence Immunity with Pseudothermal Ghost Imaging

LADAR imagers — whether classical or quantum — that are employed in clear-weather atmospheric conditions are subject to resolution loss that is due to atmospheric turbulence, i.e., the random refractive-index fluctuations that are associated with turbulent mixing of air parcels with ~1 K temperature variations [25]. Owing to its novel cross-correlation approach to image formation, it is germane to ask whether pseudothermal ghost imaging affords any immunity to this turbulence-induced resolution loss, as standard LADAR theory is not directly applicable to this case. Figure 22 shows the configuration of interest, viz., the pseudothermal ghost imaging setup from Figure 17 with atmospheric turbulence potentially present in both the signal and reference paths.[15]
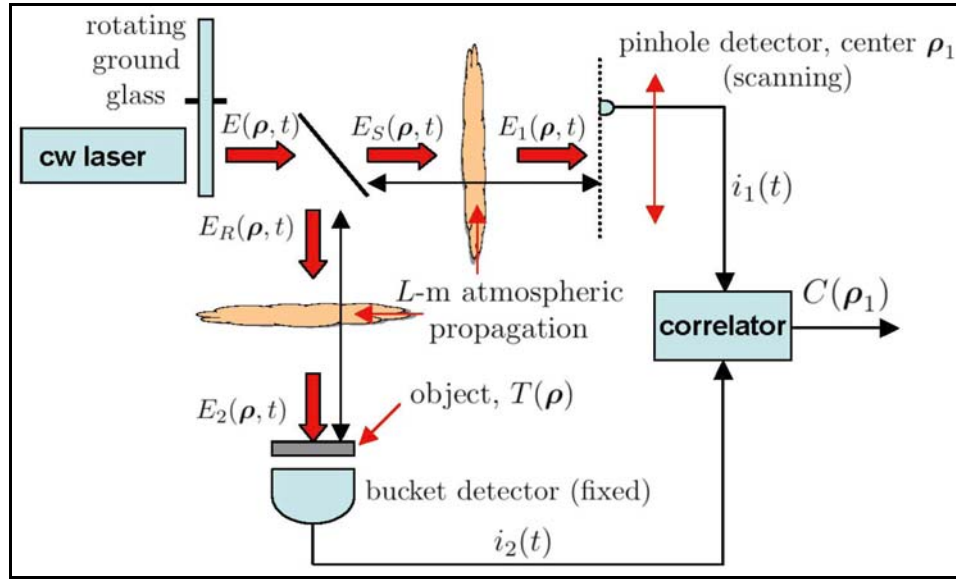
Figure 22: Pseudothermal ghost imaging in the presence of atmospheric turbulence

Using the extended Huygens-Fresnel principle [25] to account for the turbulence, we have extended our previous ghost-image resolution analysis [2] to encompass five versions of the Figure 22 scenario, namely:

1. turbulence only between the object and the bucket detector
2. identical turbulence on both the transmitter-to-bucket and transmitter-to-pinhole paths
3. statistically identical turbulence on both the transmitter-to-bucket and transmitter-to-pinhole paths
4. turbulence only between the transmitter and the bucket detector
5. turbulence only between the transmitter and the pinhole detector.

---

[15] Similar results can be developed for biphoton ghost imaging in the presence of turbulence.

The results we have obtained — for the typical far-field propagation operating regime of pseudothermal ghost imaging with a source diameter that exceeds the turbulence coherence length — are as follows.

1. There is no loss of resolution when the turbulence is only present between the object and the bucket detector.
2. There is no loss of resolution when identical turbulence is present on both the transmitter-to-bucket and transmitter-to-pinhole paths.
3. Resolution is turbulence limited when statistically identical turbulence is present on both the transmitter-to-bucket and transmitter-to-pinhole paths.
4. Resolution is turbulence limited when turbulence is only present between the transmitter and the bucket detector
5. Resolution is turbulence limited when turbulence is only present between the transmitter and the pinhole detector.

The first two cases on this list do not represent realistic operating conditions for ghost imaging in the Figure 1 LADAR scenario. It is exceedingly unlikely that the *only* turbulence to be encountered would be between the object and the bucket detector. Even more difficult to imagine is a LADAR scenario in which the exact *same* turbulence realization, i.e., the exact same amplitude and phase disturbances, would be present on the signal and reference paths. The last three cases on the preceding list are possible LADAR scenarios, but none offer immunity to atmospheric turbulence. Indeed, case 3, which is the most likely case, has a turbulence-limited resolution that is worse than those of cases 4 and 5.

3.0   ANGLE-ANGLE PROOF-OF-CONCEPT EXPERIMENTS

In this section we describe the proof-of-concept experiments undertaken at Northwestern University in support of Harris Team's sensor concept. The goal was to demonstrate two key points in our quest to achieve angle-angle resolution beyond the shot-noise-limited performance: 1) that shot-noise-limited imaging can be performed in the lab with available detector arrays and quantitative comparisons between experimental results and theoretical predictions can be made in a one-versus-two-target hypothesis testing scenario; and 2) that phase-sensitive amplification can be performed with available nonlinear crystals and pump lasers to achieve signal-gain values large enough to overcome detection-inefficiency-induced degradation in image resolution. In the latter context, theoretical work was also performed by the University of Texas, Arlington team members to enable quantitative comparisons between the experimental results and predictions of a model of the phase-sensitive parametric amplification process in a second-order nonlinear crystal pumped with an inhomogeneous beam profile.

3.1 Experimental Demonstration of a High-Gain PSA

A PSA works by amplifying only the in-phase component of the input signal and noise—while at the same time attenuating the quadrature components—and thus it is capable of preserving the signal-to-noise (SNR) of the input signal. At large gains, a PSA provides a noise factor (SNR_{out}/SNR_{in}) approaching one, which is two times better than what a phase-insensitive amplifier (PIA) can do [26]. Such a device has been shown to be useful for noise-free image amplification in previous Northwestern University experimental work [27].

In the context of resolution enhancement of an optical imaging system, the resolution is intrinsically tied to the SNR of the detected signal. Since imperfect detection (less-than-unity quantum-efficiency) degrades the measured SNR, this problem can be alleviated by the use of a PSA before detection. Phase-sensitive pre-amplification of the received signal in effect improves the overall detection efficiency of the system, as described in Section 2.3.1. More importantly, a PSA is also an indispensable component in Harris Team's quantum sensor concept involving SVI because of the rapid degradation of the squeezed vacuum in the presence of post-SVI detection losses.

The layout of the PSA imaging experiment is illustrated in Figure 23. High-extinction-ratio 1560-nm optical pulses of 160 ps pulse duration were generated at a repetition rate of 10 MHz from a homemade electronic pulse-carving system. The optical pulse train was subsequently amplified with a 5 W Erbium-doped fiber amplifier (EDFA) to produce kilowatts peak-power optical pulses [28]. The 1560 nm pulses were used to generate high peak power pulses at 780 nm via second harmonic generation (SHG) in a 20 mm periodically-poled potassium-titanyl-phosphate (PPKTP) crystal. We were able to generate close to 3 W of 780 nm beam with better than 60% conversion efficiency in the up-conversion process, as shown in Figure 24. The SHG performance was mainly limited by the nonlinear effects in the high power EDFA, which was apparent when pulses of shorter duration (higher duty cycle) were used.
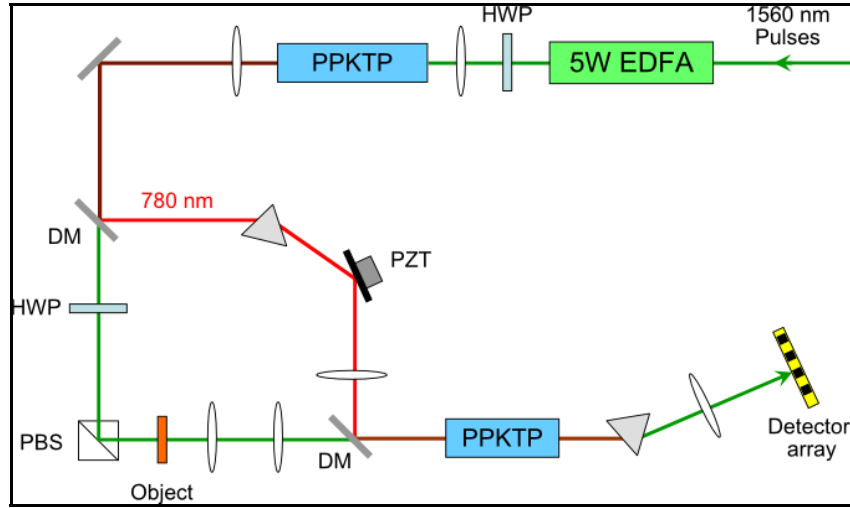
Figure 23: A schematic of the spatially-broadband PSA experiment at Northwestern University. PPKTP: periodically-poled potassium-titanyl-phosphate crystal; EDFA: Erbium-doped-fiber amplifier; HWP: half-wave plate; DM: dichroic mirror; PBS: polarizing beam splitter; PZT: piezoelectric transducer
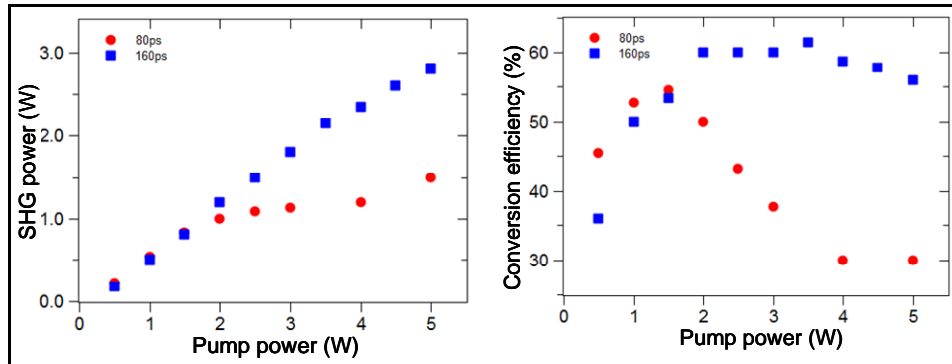
Figure 24: Left — Average harmonic power generated with a 20-mm-long PPKTP crystal vs. average pump power for different pump-pulse durations. Right — Associated conversion efficiency for the SHG process

A signal beam derived from the residual 1560 nm beam was used to illuminate a target in one arm of a Mach-Zehnder interferometer. At the exit of the interferometer, the image-bearing beam was recombined with the 780 nm pump beam after passing through a 4-f lens system. An image of the target was formed at the center of a second 20-mm-long PPKTP crystal for degenerate optical parametric amplification. The relative phase of the pump beam was actively controlled with the mirror mounted on a piezoelectric transducer so as to maintain phase sensitive amplification. The amplified image was magnified and relayed onto a Hamamatsu 1D array detector for gain measurements [29].

The performance of the optical parametric amplification was characterized by measuring the image gains when the pump beam was turned on. The pump beam was focused down to a waist size of about 40 μm at the center of the PSA crystal. No target was present at the signal path, and the waist of the collimated beam of about 800 μm was imaged onto the center of the crystal. The image profiles of the signal beam with and without phase-sensitive amplification are shown in Figure 25. Since the pump waist was smaller than the signal beam, only the overlapping region of the signal beam was amplified. The gain values of the center pixel at different pump powers are plotted in Figure 25. The data show very good agreement with the theoretical fit that took into account the effects of the inhomogeneous pump and gain-induced diffraction [30]. The gain results show that the PSA is capable of delivering more than 16 dB of peak gain at 1 kW pump peak power.
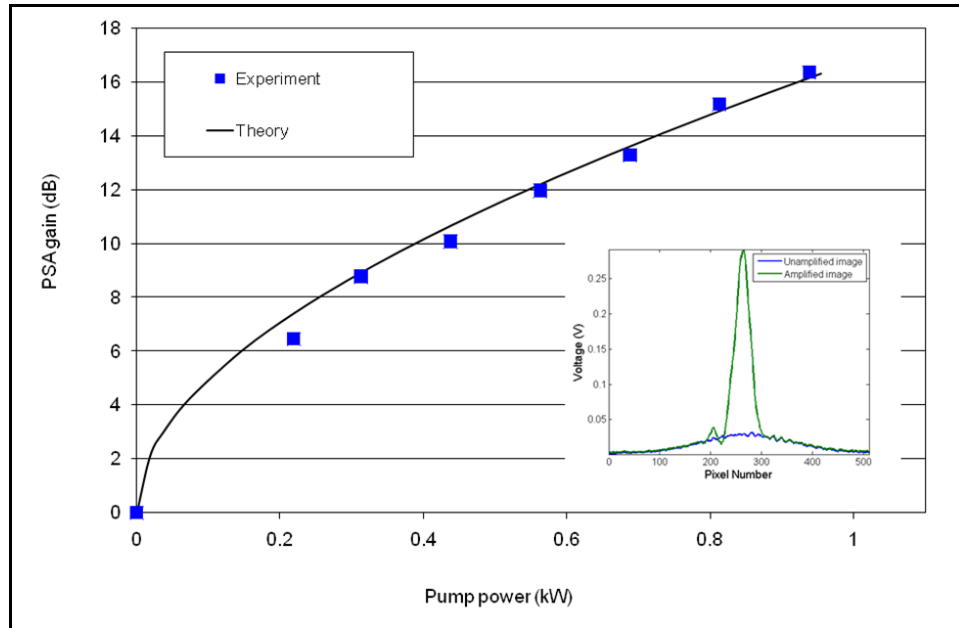

Figure 25: Peak PSA gains obtained from the 20-mm-long PPKTP crystal. Inset: 1-D spatial profiles of the input (blue trace, obtained with pump off) and amplified (green trace, obtained with pump on) Gaussian-shaped signal beam

3.2 Study of Classical Resolution Limits via Hypothesis Testing

The Quantum Sensor Program seeks improvements in both angle-angle and range resolution compared to a reference classical LADAR system. The proposed solutions entail transmission of classical states while performing non-classical detection in the receiver in the form of squeezed-vacuum injection and phase-sensitive amplification. In order to support theoretical derivations and demonstrate in principle the feasibility of such resolution enhancements in Phase 1 of the QSP, laboratory table-top experiments utilizing initially only classical transmission and detection were done. The experiments were designed in accordance with the theoretical treatment of the resolution problem. Namely, resolution improvements were treated in the context of a binary hypothesis testing problem. In the most fundamental scenario, a sensor interrogates a target and must decide whether the received signal originated from one or two targets. This is in contrast to detecting whether a target exists at all. Theoretical analysis and simulations [31], for a specular target, anticipate a scaling of resolution with signal-to-noise ratio (SNR) proportional to SNR$^{-1/4}$ for direct detection, while coherent detection improves the scaling exponent to (-1/2) for homodyne and heterodyne detection. In the case of speckle targets, the scaling for homodyne and heterodyne was shown to drop to (-3/10) [9].[16] Phase I classical hypothesis testing was meant to establish a methodology for analyzing one-dimensional resolution data in the context of a binary testing problem. The same methodology is meant to be incorporated in the more complex experiments down the road, i.e., stand-alone phase sensitive amplification and the combined squeezed-vacuum injection plus phase-sensitive amplification.

As described Section 2.3, the baseline scenario requires distinguishing between two hypotheses. The null hypothesis (H_0) assumes one target on boresight. The other hypothesis (H_1) assumes two identical targets that are symmetrically displaced about the boresight that return the same number of signal photons to the LADAR as the single target. Thus, the decision is independent of the total number of photons seen by the receiver in each scenario, and it is assumed that the two hypotheses are equally likely. The hypothesis testing criterion is then derivable from Bayes' rule with the appropriate photon probability distribution functions. For a relatively large photon flux, we implement a Gaussian distribution for the photon statistics, rather than a Poissonian distribution. The detection device used was an InGaAs linear array (Andor Technologies) of 512 discrete pixels (50 μm pitch) denoted as a discrete set, $\{x_i \in [x_{1,\ldots,}x_N]\}$. Each pixel in the detector array has noise that is comprised of two contributions. The dark noise ($\sigma_d^2(x_i)$) describes the noise from the detection system itself (dark current and load-resistor thermal noise), and is independent of the light level impinging on each pixel. The second contribution ($\sigma_\ell^2(\mu(x_i))$) is due to the statistical nature of the light and the excess noise from the coherent light source.

---

[16] Unlike the case described in Section 2.3, the initial proof-of-principle hypothesis testing experiments were performed with specular, rather than speckle, targets.

$$\sigma^2(x_i) = \sigma_d^2(x_i) + \sigma_\ell^2(\mu(x_i))$$
$$\sigma_\ell^2(\mu(x_i)) = \sigma_{SN}^2(\mu(x_i))[1 + C\sigma_{SN}^2(\mu(x_i))]$$

(28)

where x_i denotes the individual pixels in the detector array, and $\mu(x_i)$ is similar to the rate function denoted in [32]. We neglect the explicit time dependence of the rate functions which is embedded in the experimental data as the detector's integration time. The constant C was found from a quadratic fit to the excess noise measured in our coherent source.

The following are the probability distributions that were used and the resulting criterion. P are the a-priori probabilities for each event, $\mu(x)$ are the spatially dependent measured mean values at each pixel and $\sigma(x)$ are the associated variances. Both the means and the variances are assumed to be known prior to data collection. The analyzed data is denoted r_i.

$$\frac{P_0}{\left(2\pi\sigma_0^2(x_i)\right)^{1/2}}\exp\left[-\left(r_i - \mu_0(x_i)\right)^2\big/2\sigma_0^2(x_i)\right] = \frac{P_1}{\left(2\pi\sigma_1^2(x_i)\right)^{1/2}}\exp\left[-\left(r_i - \mu_1(x_i)\right)^2\big/2\sigma_1^2(x_i)\right]$$

(29)

$$\sum_i^N\left[\frac{1}{2}r_i^2\left(\frac{1}{\sigma_0^2(x_i)} - \frac{1}{\sigma_1^2(x_i)}\right) + r_i\left(\frac{\mu_1(x_i)}{\sigma_1^2(x_i)} - \frac{\mu_0(x_i)}{\sigma_0^2(x_i)}\right)\right] \overset{H_1}{\underset{H_0}{\gtrless}} \frac{1}{2}\sum_i^N\left[\frac{\mu_1(x_i)^2}{\sigma_1^2(x_i)} - \frac{\mu_0(x_i)^2}{\sigma_0^2(x_i)} - \ln\left(\frac{\sigma_0(x_i)}{\sigma_1(x_i)}\right)\right]$$

In the classical hypothesis testing experiments, a USAF resolution plate served as a target. Desired spatial resolutions were chosen and imaged one-to-one in transmission onto the array detector. Prior to data collection, we thoroughly investigated the noise characteristics of the detector. This investigation established the uniformity of the array and verified that each pixel's noise process was independent of neighboring pixels. A schematic of the experimental setup is depicted in Figure 26.
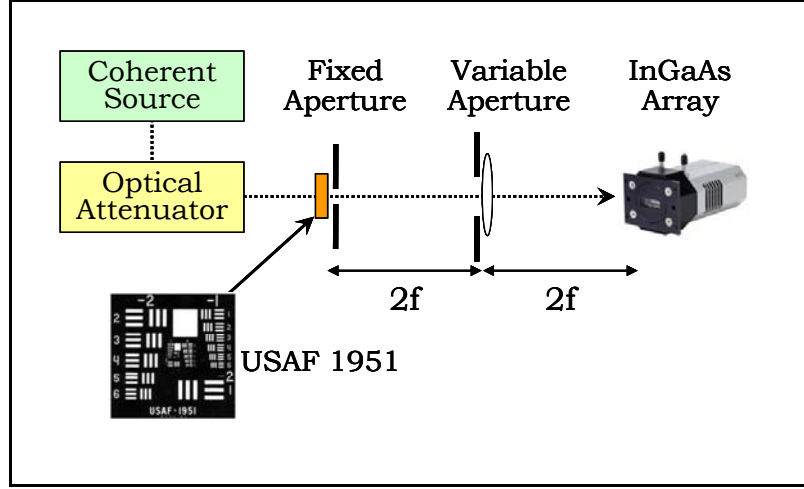
Figure 26: Classical hypothesis testing configuration

Measurements from this setup could provide the error rates with which a certain target is discerned as a function of SNR, but more importantly, the scaling of resolution versus SNR can be measured. By keeping a desired error probability fixed and examining the required SNR to reach a given resolution level, such scaling can be directly obtained. In this particular case, the use of a USAF 1951 resolution does not allow sampling of relatively high spatial frequencies. Alternatively, one can choose a set of slits on the resolution target corresponding to only one spatial frequency, while varying an aperture in front of the imaging lens. The resolution, relative to the Rayleigh limit, was defined as d/d_R where d is the separation between the slits on the USAF target, and d_R is the Rayleigh limit of the imaging configuration, $d_R = 2\lambda f/D$, with f being the focal length of the lens, λ being the center wavelength and D the lens' aperture. The parameter D was varied via a micrometer controlled slit that facilitated collecting data below the Rayleigh limit. For desired values of D, the optical power impinging on the target was adjusted to maintain a fixed error probability, typically $P_E = 10^{-2}$. SNR was calculated once the power level was properly set according to the definition

$$SNR = \frac{\left(\sum_{i=1}^{N} n_i\right)^2}{\sum_{i=1}^{N} \left\langle \Delta n_i^2 \right\rangle} \tag{30}$$

where, n_i is the photon number at pixel i. Below are experimental results for the scaling of resolution versus SNR for direct detection. Statistical analysis was performed with 55,000 events at each power level. SNR fluctuations were extremely small as seen in Figure 27 such that the uncertainties are smaller than the data points. The dashed line in Figure 27 uses theoretical scaling, and further simulations revealed that the scaling exponent for direct detection (-1/4) held for both signal shot-noise and dark noise limited cases, and also occurred both for finite slit widths and point targets. This scaling law only broke down in the very low SNR regime (SNR <5 dB), in which case the scaling indeed depended on the details of the target statistics and shape.
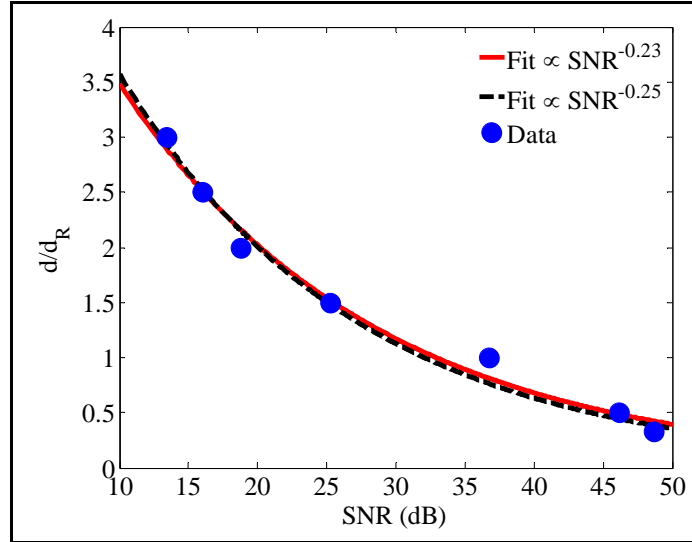

Figure 27: Classical hypothesis testing results for direct detection

3.3 Theory Support for PSA Experiments

A theoretical effort was undertaken to support PSA experiments directly by modeling signal propagation within the PSA. One of the most important tasks is that of maximizing the number of amplified modes (i.e., pixels) for a given pump power.

A spatially-broadband PSA pumped by a plane wave can be described by an analytical model, which makes the PSA essentially equivalent to an active low-pass or band-pass filter in the spatial frequency domain (i.e., the behavior is described by a modulation transfer function or MTF). However, any practical pump beam has a finite spatial size and typically a Gaussian spatial profile (spatially-inhomogeneous pump). This finite Gaussian profile breaks the shift invariance symmetry of the PSA and makes the spatially-broadband PSA pumped by a Gaussian beam impossible to describe in terms of an MTF. In addition, no analytical solution is known for such a PSA with finite bandwidth. Thus, our theoretical approach has been to gain physical insights from analytical plane-wave theory and then extend this intuition into the numerical modeling of the realistic inhomogeneous pump cases. [33]

The main physical insight obtained from the plane-wave-pump theory is the range of spatial frequencies that can be amplified, i.e., the spatial bandwidth of the PSA. [34],[35] The gain of a phase-insensitive optical parametric amplifier of length L with plane-wave pump is given by

$$G_{\mathrm{PIA}} = |\mu(q)|^2 = 1 + |\nu(q)|^2 = 1 + \frac{\sinh^2(\kappa L\sqrt{1-r^2})}{1-r^2},$$ (31)

where we introduced phase mismatch factor r as a function of spatial frequency $q=2\pi f$:

$$r = \frac{\Delta k_{\mathrm{eff}}}{2\kappa} = \frac{1}{2\kappa}\left[\Delta k + \frac{q^2}{2}\left(\frac{1}{k_s} + \frac{1}{k_i}\right)\right],$$ (32)

with

$$\kappa^2 = \kappa_s\kappa_i = \frac{\omega_s\omega_i d_{\mathrm{eff}}^2 I_p}{2\varepsilon_0 n_s n_i n_p c^3}.$$ (33)

The PSA gain is given by

$$G_{\mathrm{PSA}} = \left\| \mu(q)| + e^{2i\left(\theta_s^{opt}-\theta_s\right)} |\nu(q)\right\|^2 = \left|\sqrt{G_{\mathrm{PIA}}} + e^{2i(\theta_s^{opt}-\theta_s)}\sqrt{G_{\mathrm{PIA}}-1}\right|^2,$$ (34)

where θ_s is the signal phase at the input, and the optimum input signal phase for maximum phase-sensitive gain is given by

$$\theta_s^{\mathrm{opt}} = \frac{\pi}{4} + \frac{1}{2}\tan^{-1}\left[\frac{r}{\sqrt{1-r^2}}\tanh(\kappa L\sqrt{1-r^2})\right]$$
$$+ \frac{1}{2}\arg\left[\frac{1}{\sqrt{1-r^2}}\sinh(\kappa L\sqrt{1-r^2})\right].$$ (35)

The PIA and PSA gains are plotted in Figure 28 (left) for the parameters of the ongoing PSA experiment (with Δk=0). Figure 28 also shows the optimum signal phase Eq. (35) (normalized by π) versus spatial frequency. For $r \geq 1$, the sinh function in Eqn. (31) becomes a $i$sin function (which leads to $1+(\kappa L\mathrm{sinc})^2$ function for gain), and for $r = 1$ we have $G_{\mathrm{PIA}} = 1 + (\kappa L)^2$. The first zero of sinc function—also being the first zero of $\nu(q)$— occurs at

$$f_0 = \sqrt[4]{\frac{k_s^2}{4\pi^2}\left(\frac{\kappa^2}{\pi^2}+\frac{1}{L^2}\right)},$$

(36)

which can be approximated as

$$f_0 \approx \sqrt{\frac{k_s}{2\pi L}} \quad \text{for } \kappa L \ll 1,$$

(37)

$$f_0 \approx \frac{1}{\pi}\sqrt{\frac{k_s \kappa}{2}} \quad \text{for } \kappa L \gg 1.$$

(38)

All previous papers have used $q \sim \sqrt{k_s / L}$, originating from Eq. (37), as an estimate for the spatial bandwidth and its scaling with L. The estimates given by Eqs. (36)–(38) are plotted in Figs. 28 and 29 and compared to the actual 3-dB bandwidths of PIA and PSA gains expressed by Eqs. (31) and (34), respectively. The left portion of Figure 28 shows OPA gain versus spatial frequency $f = q/2\pi$ for parameters of the ongoing Northwestern experiment. The right portion of Figure 28 shows the spatial bandwidth $f_c = q_c/2\pi$ of a 25-mm-long KTP-based OPA at 1550 nm signal wavelength, as a function of the PIA gain at zero spatial frequency. Also shown in Figure 28 is the optimum signal phase maximizing the PSA gain. An arrow in the left figure indicates the location of the first zero of $\nu(2\pi f)$ function. Labels "PSA opt.," "PIA, and "PSA $\pi/4$" in Figure 28 correspond to –3-dB bandwidths of PSA with optimum signal phase, PIA, and PSA with $\theta_s = \pi/4$ signal phase, respectively. Thick red line corresponds to the location of the first zero of $\nu(2\pi f)$. Dashed red lines are its asymptotes for low and high pump powers. The traditional estimate of spatial bandwidth corresponds to the low-power asymptote $\sqrt{k_s/(2\pi L)}$ (horizontal dashed red line).
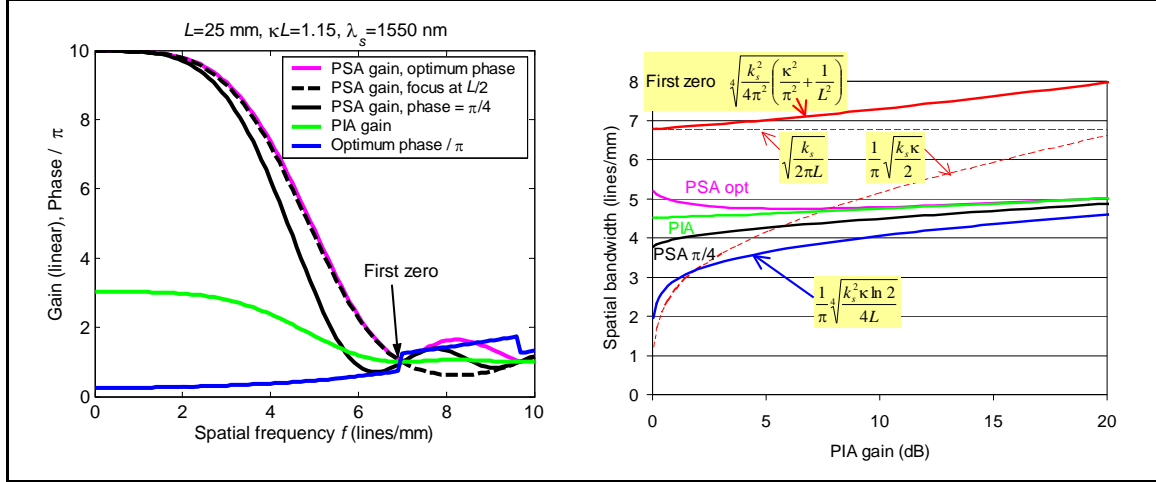
Figure 28: Left — OPA gain versus spatial frequency. Right — Spatial bandwidth as a function of the PIA gain at zero spatial frequency

An alternative way to estimate the 3-dB bandwidth for large pump powers (i.e., large κ) is to note that the sinh function becomes an exponential function at high gains, i.e.,

$$G_{\text{PIA}} \approx \frac{\exp(2\kappa L\sqrt{1-r^2})}{4(1-r^2)} \approx \frac{1}{4}\exp(2\kappa L)\exp(-\kappa L r^2) ,$$

(39)

and at the 3-dB bandwidth f_c we have

$$\exp(-\kappa L r^2) = \frac{1}{2} ,$$

(40)

or

$$f_c = \frac{1}{\pi}\sqrt[4]{\frac{k_s^2 \kappa \ln 2}{4L}} .$$

(41)

The estimates calculated from Eq. (41), also plotted in Figs. 28 and 29, are very accurate at high gains. One can also see that even at low gains Eq. (41) provides a closer and more conservative value to the actual bandwidth than Eqs. (36)–(38). The spatial bandwidth dependence on L is shown in Figure 29 (left).

Also note that for small values of κL, optimum signal phase Eq. (35) is

$$\theta_s^{\text{opt}} \approx \frac{\pi}{4} + \frac{\kappa L r}{2} = \frac{\pi}{4} + \frac{\Delta k L}{4} + \frac{q^2}{4k_s}L ,$$

(42)

i.e., signal phase is obtained by placing the focus of the image at $z_0 = L/2$ (middle of the crystal). The PSA gain for such a focused beam is also plotted in Figure 28, and one can see that the difference between this resultant gain and optimum PSA gain is negligible. The difference between the actual optimum signal phase Eq. (35) and the approximate phase Eq. (42) is plotted in Figure 29 (right) for several values of the PSA gain at zero spatial frequency. The left portion of Figure 29 shows spatial bandwidths $f_c = q_c/2\pi$ of a KTP-based OPA at 1550 nm as a function of crystal length L for a fixed pump power (κ = 0.046 mm^{-1}, which corresponds to 10 dB PSA gain for L = 25 mm). Color coding and other notations are the same as those in the right portion of Figure 28. The right portion of Figure 29 plots the difference between the actual optimum signal phase (Eq. 35) and the approximate phase (Eq. 42) for various values of the PSA gain at zero spatial frequency. The last point on each curve corresponds to the first zero of $\nu(2\pi f)$.
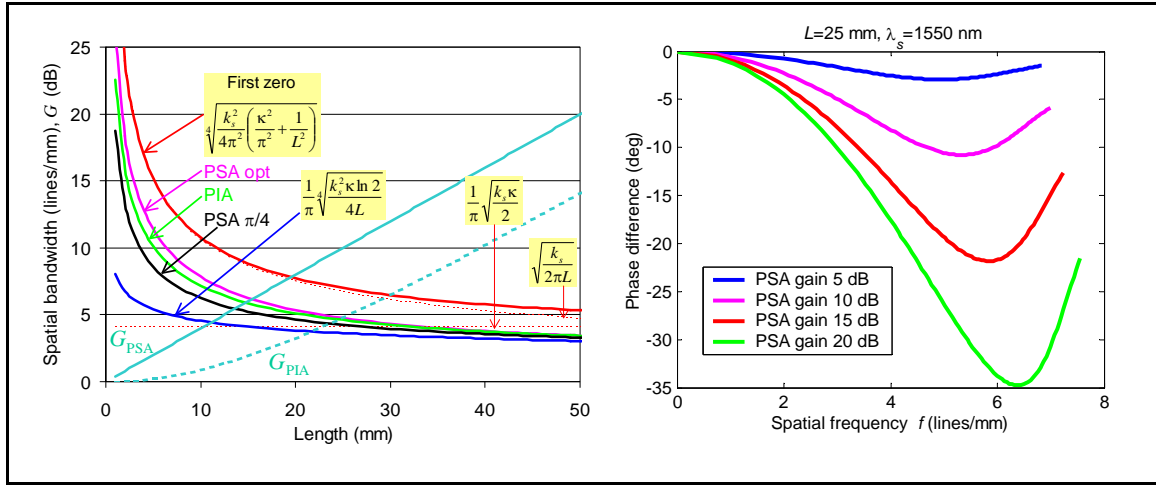

Figure 29: Left — Spatial bandwidths of an OPA at 1550 nm as a function of crystal length. Right — Difference between the actual optimum signal phase and the approximate phase for various values of the PSA gain at zero spatial frequency

Although the plane-wave-pump approach is not applicable to real PSAs, it provides some qualitative insights into the performance that can be expected from these devices. In particular, the plane-wave theory estimates given by Eqs. (36)–(38) and (41) for the PSA's spatial bandwidth can be multiplied by the size of the real pump beam to estimate the number of spatial modes amplified in each dimension. This approach leads to an important conclusion that the total number of amplified modes (pixels) is proportional to the total pump power. See references [36],[37].

To predict propagation of an image through a realistic PSA, we have developed and applied a 3D numerical modeling tool based on the split-step Fourier method (also known as FFT-BPM). We have carefully verified this model against PSA experimental gain measurements taken at various pump powers, and found good quantitative agreement (see Figure 25). Next, we have optimized the pumping configuration to maximize the number

of amplified modes (pixels) for a given pump power [37],[38]. For example, Figure 30 shows the input and amplified text image at 1560 nm, experiencing both total-power and peak gains of ~10 dB at 10-kW pump power in a 25-mm-long KTP crystal. Here, image size is ~220×90 μm^2 and the optimized elliptical-Gaussian pump spot size is 300×35 μm^2 (at 1/e intensity radius). The vertical scale is linear and normalized by the peak intensity of the input image. The horizontal scale is in arbitrary units. In Figure 30, images (b) and (d) are the top views of (a) and (c), respectively, and (e) is the front-side view of (c).

From Figure 30(e) one can see that the text image is clearly recognizable, with even the peripheral portions of the text experiencing gain in excess of 6 dB. In the plane-wave approximation, the diameter of the PSA's point-spread function can be roughly estimated as ~ $[L/(2\pi k_s)]^{1/2}$ = 23 μm from the inverse of the crystal's spatial phase-matching bandwidth, although the underlying approximation tends to overestimate the spatial bandwidth, as pointed out above. For an inhomogeneous pump of a given spot size, the number of amplified pixels can be approximated by the ratio of the pump-beam area $\pi a_{0px}a_{0py}$ and the effective pixel area $L/(8k_s)$ of the plane-wave-pump case, which gives ~80 effective pixels of resolution in our chosen example. This order-of-magnitude-accurate number of amplified pixels roughly agrees with the estimated number of observed amplified pixels found by counting the number of dark and bright lines in x and y dimensions in (d), which is at least 12×5=60 pixels. In our optimizations, we have also investigated the impacts of Guoy phase on the PSA gain, finding that this phase makes the optimum signal phase slightly different from that expected from the plane-wave-pump theory. This phase deviation is particularly important for the de-amplified quadrature.
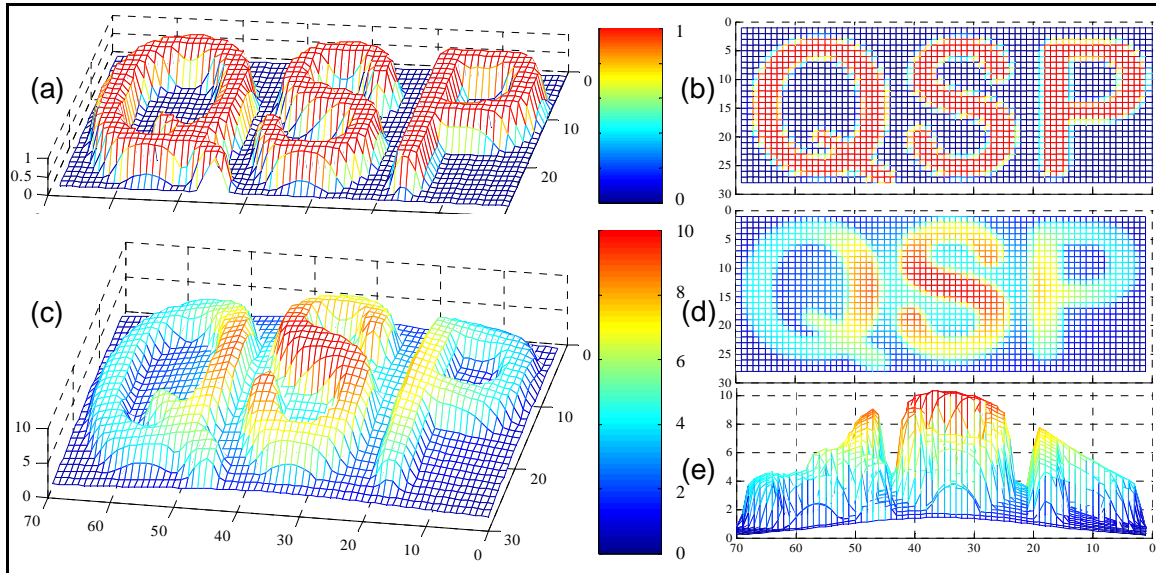

Figure 30: Intensity image before (a, b) and after (c, d, e) amplification by the PSA

54

To summarize, we have used a plane-wave theory to develop an improved estimate of the PSA's spatial bandwidth. We have found that the conditions for an optimum input signal phase profile are approximately satisfied by simply placing the image focus at the middle of the crystal. We have applied these insights to optimize image amplification in a PSA with a finite-size pump, and obtained gains between 6 dB and 10 dB for over 60 pixels at 10-kW pump power. This computation has been accomplished with a specially-developed PSA numerical solver, which has proven to be *quantitatively* accurate in comparisons with PSA experimental data. Furthermore, for calculations of noise evolution in the PSA, we have developed a Green's-function formalism yielding noise correlation functions at the output of a PSA with arbitrary pump profile. [33]

4.0 RANGE PROOF-OF-CONCEPT EXPERIMENTS

In standard optical coherence tomography (OCT) the range resolution is determined by the spectral bandwidth of the probe pulses and is ultimately limited by dispersion in the pulse propagation medium. Quantum optical coherence tomography (Q-OCT) utilizes entangled photon pairs from spontaneous parametric downconversion (SPDC) to demonstrate a factor of two improvement in axial resolution with even-order dispersion cancellation [39],[40]. Erkmen and Shapiro [1] have shown theoretically that the measurement advantages of Q-OCT do not derive from entanglement but rather from the phase-sensitive cross correlation between the signal and idler light. Moreover, based on this discovery, they proposed a new technique, called phase-conjugate optical coherence tomography (PC-OCT) [1], that uses classical resources with an unconventional, but still classical, receiver to achieve the same factor-of-two resolution enhancement and even-order dispersion cancellation as Q-OCT. In the context of target ranging in the Quantum Sensors Program the PC-OCT concept is a Type-2 quantum sensor, which we shall more appropriately refer to as phase-conjugate ranging (PCR).

The basic idea of PCR is shown in Figure 3 of Section 2.0. A classical transmitter sends a probe pulse to interrogate the target and the reflected pulse is fed into a phase-conjugate amplifier that generates an amplified phase-conjugate probe pulse. The amplification overcomes the losses in the probe pulse transmission and phase conjugation provides the necessary spectral phase reversal to compensate dispersion. The phase-conjugate probe pulse is transmitted to the target for a second round of interrogation before the returned pulse is mixed with a reference pulse for detection. The goal of the PCR proof-of-concept demonstration in Phase I of the Quantum Sensors Program was to verify the factor-of-two axial resolution improvement and the dispersion cancellation, relative to a standard OCT arrangement.

4.1 Transmitter and Phase-Conjugate Amplifier Characterization

There are two key components for implementing PCR. The first device is a classical transmitter that generates the reference and probe beams with phase-sensitive cross correlation, and the second device is a phase-conjugate amplifier. In our experiment the transmitter was a parametric downconverter based on a 20-mm-long periodically poled MgO-doped lithium niobate (PP-MgO:LN) crystal. Pumped by 50-ps pulses at 780 nm with a repetition rate of 31 MHz, the parametric downconverter generated reference and probe outputs centered at 1560 nm. The phase-sensitive cross correlation between the two outputs was utilized for interferometric measurements at the receiver. Figure 31 shows the spectral brightness (measured at the output of a single mode fiber) of the downconverter's fiber-coupled output at 1550 nm as a function of the average pump power. The exponential growth at high pump power indicates amplification of the spontaneously emitted outputs. SPDC is often used for generating entangled photons at low flux, typically with a mean photon pair number of much less than unity per pulse. In our case, at a spectral brightness of 1 nW/nm the transmitter output in our setup contained ~250 photons per pulse that was far brighter than an SPDC entangled photon source. At

this brightness level the transmitter outputs behaved classically.   Figure 32 displays the measured power spectrum of the parametric downconverter outputs, showing a large phase-matching bandwidth of 143 nm. The dashed line in Figure 32 is a theoretical phase-matching curve obtained from the Sellmeier equation. The large bandwidth afforded the flexibility to choose the appropriate measurement wavelengths and bandwidths. We chose a reference wavelength of 1550 nm and a probe wavelength of 1570 nm with a bandwidth of 0.36 nm for resolution improvement measurements. For dispersion cancellation measurements we used a larger bandwidth of 5 nm.
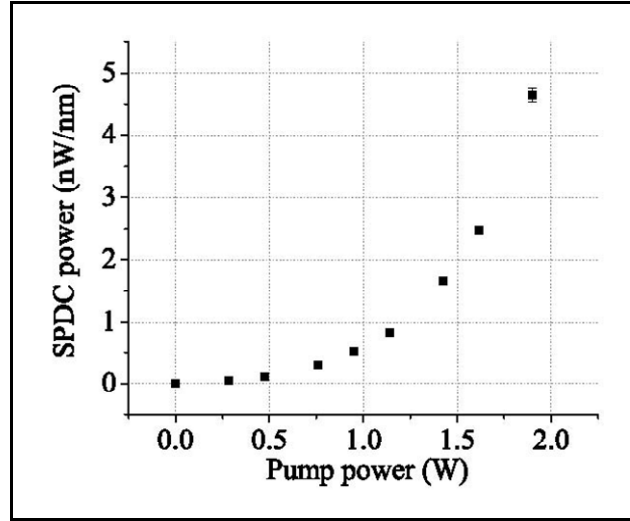

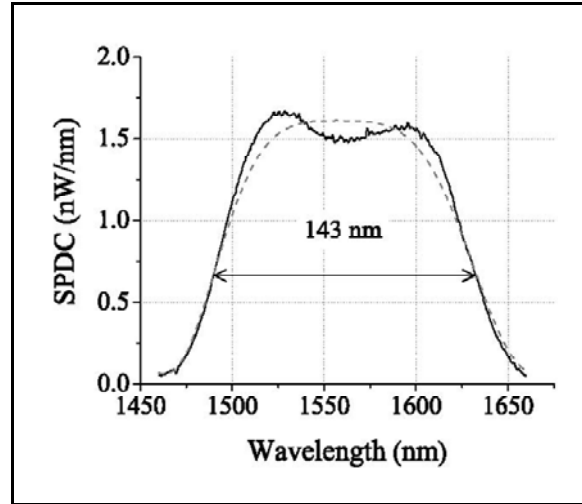**Figure 31: Spectral brightness of optical parametric downconverter as a function of pump power**

Figure 32: Power spectrum of parametric downconverter output

57

The phase conjugate amplifier was an optical parametric amplifier (OPA) based on a 20-mm-long PP-MgO:LN crystal and pumped by the same pulsed 780-nm laser that was used for the transmitter downconverter. The OPA was used to generate a 1550-nm phase-conjugate beam from the returned probe beam at 1570 nm and to provide gain. Figure 33 shows the OPA gain as a function of the average pump power, achieving a gain of nearly 20 dB at a pump power of 2 W. More details on the OPA performance including the theoretical model used for the calculation displayed in Figure 33 can be found in a technical memorandum on the OPA [41]. The dashed curve in Figure 33 is derived from a theoretical calculation that assumes an effective peak power level that is 60% of the estimated power. We attribute the power reduction to pulse broadening due to self-phase modulation.
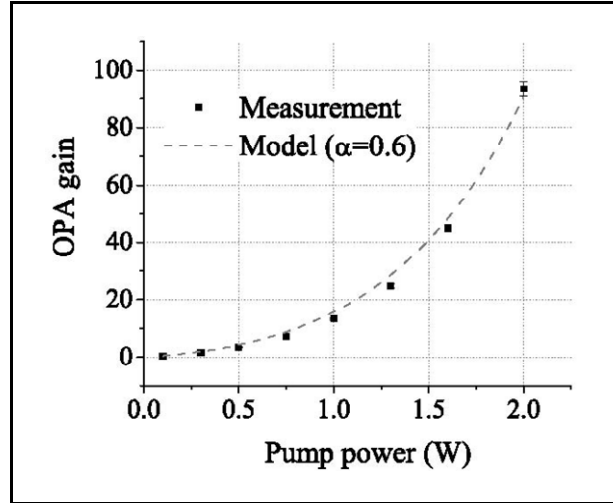

Figure 33: Optical parametric amplifier gain as a function of pump power

4.2 Baseline Classical OCT Measurements

We performed baseline measurements using a classical OCT setup, as shown in Figure 34. The transmitter (SPDC) reference and probe outputs were separated using a coarse wavelength division multiplexer (CWDM) and directed into a reference channel centered at 1550 nm and a probe channel centered at 1570 nm. We sent the probe to the target, which was a highly reflective mirror mounted on a translation stage. The reflected probe was supplied as the input to the OPA to generate an amplified phase-conjugate beam at 1550 nm, matching the reference wavelength exactly. The reference beam was retroreflected from a mirror located on a moveable stage that acted as a delay line, so that the reference pulse and the phase-conjugate probe pulse could be temporally matched. Interferometric measurements using a fiber 50-50 beam splitter were made as a function of the reference mirrorposition.
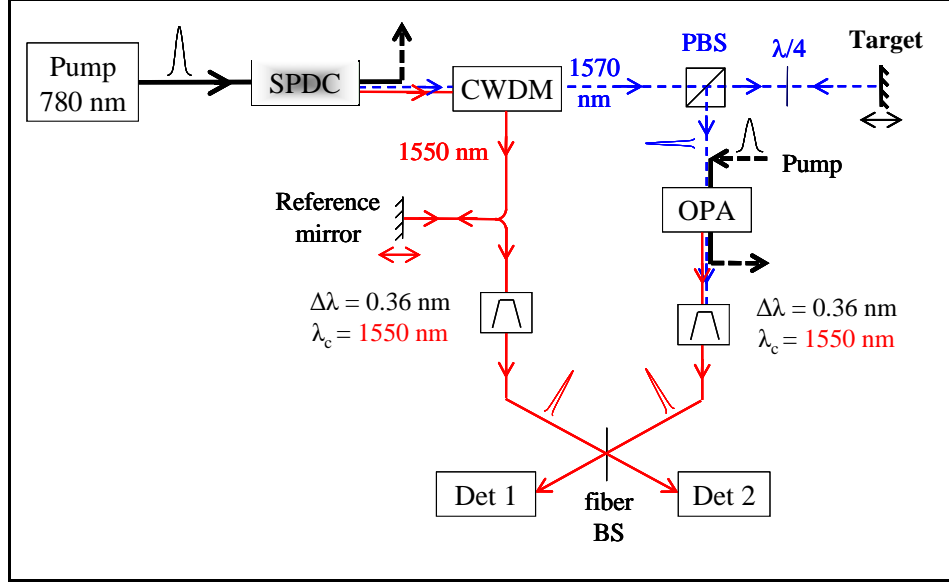
Figure 34: Schematic of the setup for classical OCT baseline measurements

Figure 35 shows the results of interferometric measurements for two different target positions separated by 2.35 mm. At each target position the reference mirror was moved over small distances and the maximum and minimum powers of the reference-probe interference envelope were recorded. The envelope contrast C is obtained from

$$C = \frac{P_{\max} - P_{\min}}{P_{\max} + P_{\min}}, \tag{43}$$

where $P_{\max}$ and $P_{\min}$ are the maximum and minimum measured power levels. The average measured axial resolution based on the two curves in Figure 35 was 2.39 mm.

We calculated the expected axial resolution as follows. (Details can be found in a technical memorandum [42].) The bandpass filter was measured to have a double-Lorentzian filter shape with a full width at half maximum (FWHM) bandwidth of 0.36 nm. By approximating the pulse shape of the probe and reference pulses to be the Fourier transform of the bandpass filter spectrum, we obtained the envelope contrast C based on the convolution of the reference and probe pulses:

$$C(z_R) = C_0 \left(1 + \sqrt{2}\pi \frac{\Delta \nu}{c} |z_R| \right) \cdot \exp\left(-\sqrt{2}\pi \frac{\Delta \nu}{c} |z_R| \right), \tag{44}$$

where z_R is the reference mirror translation from the center and $\Delta v = 45$ GHz is the frequency bandwidth of the 0.36-nm bandpass filter. The dashed curves in Figure 35 are the theoretical fits from Eq. (44), showing excellent agreement between theory and measurements. Reference mirror shift was measured to be 2.36 mm in good agreement with the target positional shift of 2.35 mm. The single-pass classical OCT measurements clearly show that the target positional shift was equal to the reference positional shift, and the resolution was limited by the pulse widths of the reference and probe beams.

Figure 35: Envelope contrast of interferometric measurements between reference and probe as a function of the reference mirror delay for two target positions

4.3 Phase-Conjugate Ranging Measurements without Dispersion

To implement the PCR experimental setup we modified the classical OCT setup of Figure 34 to include a second CWDM module for routing the phase-conjugate probe to interrogate the target a second time, as shown in Figure 36. The same transmitter outputs for the probe and reference beams were used to facilitate a direct comparison with the baseline classical OCT measurements. The purpose of the double-pass configuration was to obtain a factor-of-two axial resolution improvement. Dispersion in this setup was negligible.
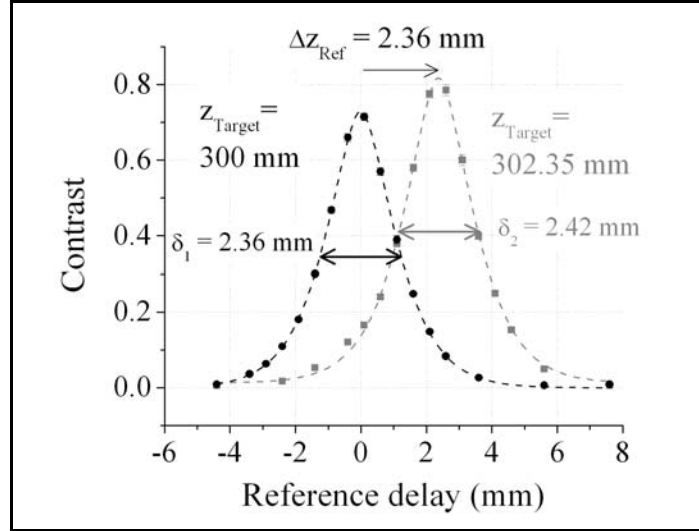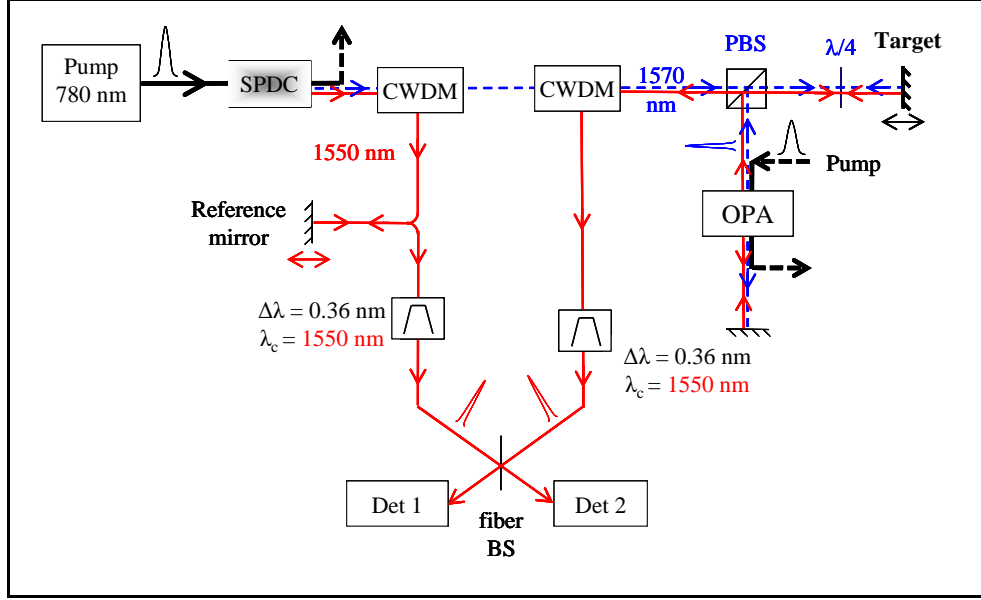
Figure 36: Schematic of setup for PCR measurements
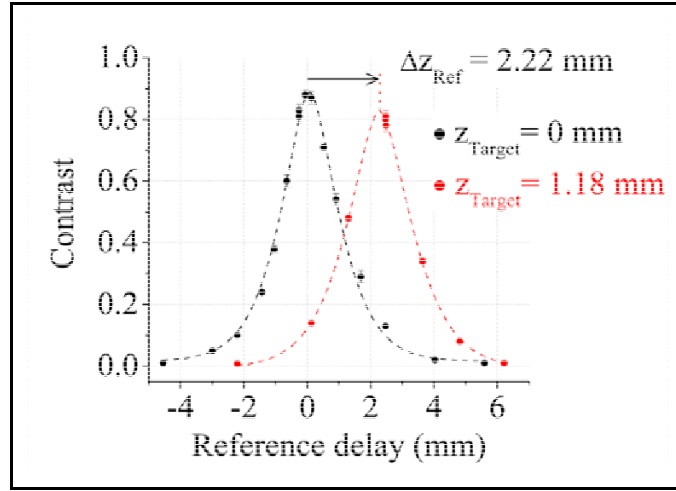

Figure 37: Envelope contrast of interferometric measurements between reference and probe as a function of reference mirror delay for two target positions

Figure 37 shows the results of the PCR measurements using probe and reference pulses set by the 0.36-nm bandpass filters. For a target positional shift of 1.18 mm, the measured reference mirror shift was 2.22 mm, or a factor of two larger within experimental uncertainties. With the same measurement bandwidth of ~2.39 mm, the PCR measurements clearly indicate that for the same amount of reference mirror travel, PCR allows target positional detection at half the amount of the travel. This measurement constitutes an axial resolution improvement of a factor of two relative to the classical OCT technique. Dashed lines in Figure 37 are theoretical fits based on Eq. (44).

4.4 Phase-Conjugate Ranging Measurements with Dispersion

The PCR measurements in Section 4.3 used a narrow 0.36-nm bandpass filter so that dispersion due to the small length of SMF28 single-mode optical fiber is negligible. Industry specification of SMF28 fibers shows a dispersion value of 17 ps per kilometer of fiber per nanometer of bandwidth. For 0.36 nm bandwidth and 10 meters of fiber, the estimated dispersive broadening amounts to only 0.06 ps, which is small compared with a pulse width of ~10 ps.

We chose to test the dispersion cancellation property of PCR by increasing the filter bandwidth to 5 nm with the corresponding pulse width of ~0.8 ps, or a spatial coherence length of 0.24 mm. The probe arm had a total SMF28 fiber length of ~51 meters, and PCR dispersion cancellation would only occur for the length of fiber within the double-pass configuration of the probe arm. Because dispersion could not be corrected in the reference arm, we used a dispersion-shifted fiber wherever possible, comprising ~37 meters of such fiber with a dispersion coefficient of 4 ps/km/nm. Figure 38 shows a typical interferometric envelope with a measured width of 0.38 mm. This measurement is in good agreement with our model, taking into account the dispersion in the reference arm and the small uncompensated section in the probe arm. As a comparison, if dispersion cancellation were absent, the measured width would have been 0.78 mm.
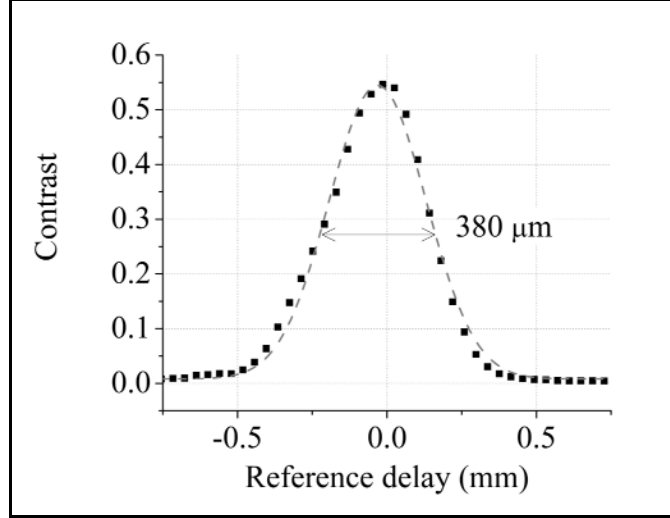
Figure 38: Envelope contrast of interferometric measurements between reference and probe as a function of reference delay for 0.8-ps pulses

Figure 39 shows the same PCR measurements for six target positions with 0.10-mm separation between adjacent target locations. The average measured reference mirror displacement between adjacent targets is 0.225 mm, which is in agreement with the expected value of 0.20 mm, thus demonstrating the factor-of-two axial resolution improvement of PCR with dispersion cancellation. The variations in reference mirror displacements were due to temperature fluctuations that led to variations in fiber lengths and hence shifts in the temporal overlap between the reference and probe pulses. In principle, this effect could be avoided by stabilizing the temperature of the entire optical fiber setup, or by operating the system in free space. The PCR measurements using subpicosecond pulses thus verify the basic concept of PC-OCT showing a factor-of-two improvement in axial resolution with dispersion compensation [1].
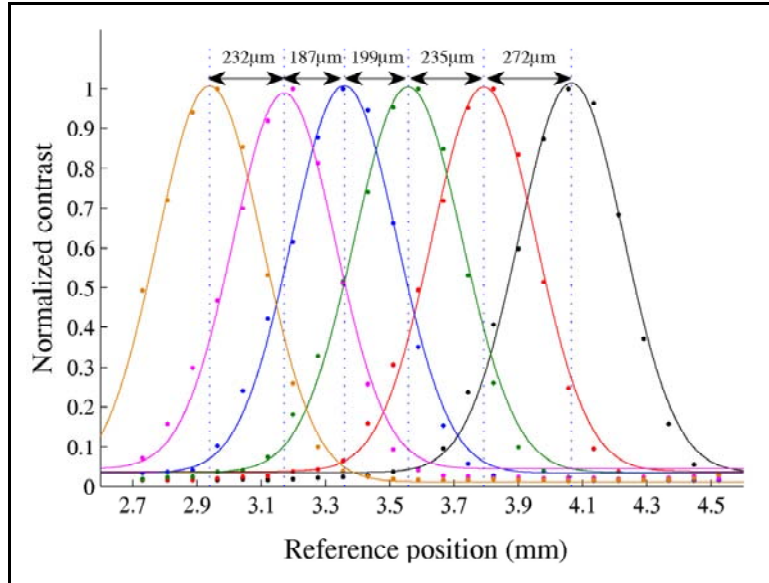
Figure 39: Envelope contrasts and Gaussian fits (solid lines) of interferometric measurements between reference and probe as a function of reference mirror delay

5.0   TYPE-2 LADAR CONCEPT

The quantum imaging LADAR sensor described previously can enhance the angular resolution — over a conventional sensor — by recovery of some of the high-spatial-frequency content rejected by a soft aperture (using locally generated squeezed vacuum) and by recovery of lost image information caused by low quantum efficiency of the detector array (using receiver-side phase-sensitive amplification). The LADAR will function as a Type-2 quantum sensor (classical illumination and interaction with the target, but quantum detection).

Figure 40 shows the preliminary layout of the proposed LADAR showing quantum PSA and SVI and bistatic illumination of a target. The shaded region enclosed with a dashed line depicts the QIE function provided by phase-sensitive amplification (right) and squeezed-vacuum injection (far left). The local oscillator, necessary for homodyne operation, is generated within the shaded region. A classical LADAR baseline would be created by blocking the QIE functionality of both the PSA and the SVI. A portion of the generated beam (lower left) is picked off from the QIE section, amplified and used to illuminate a target as in conventional classical LADAR operation.
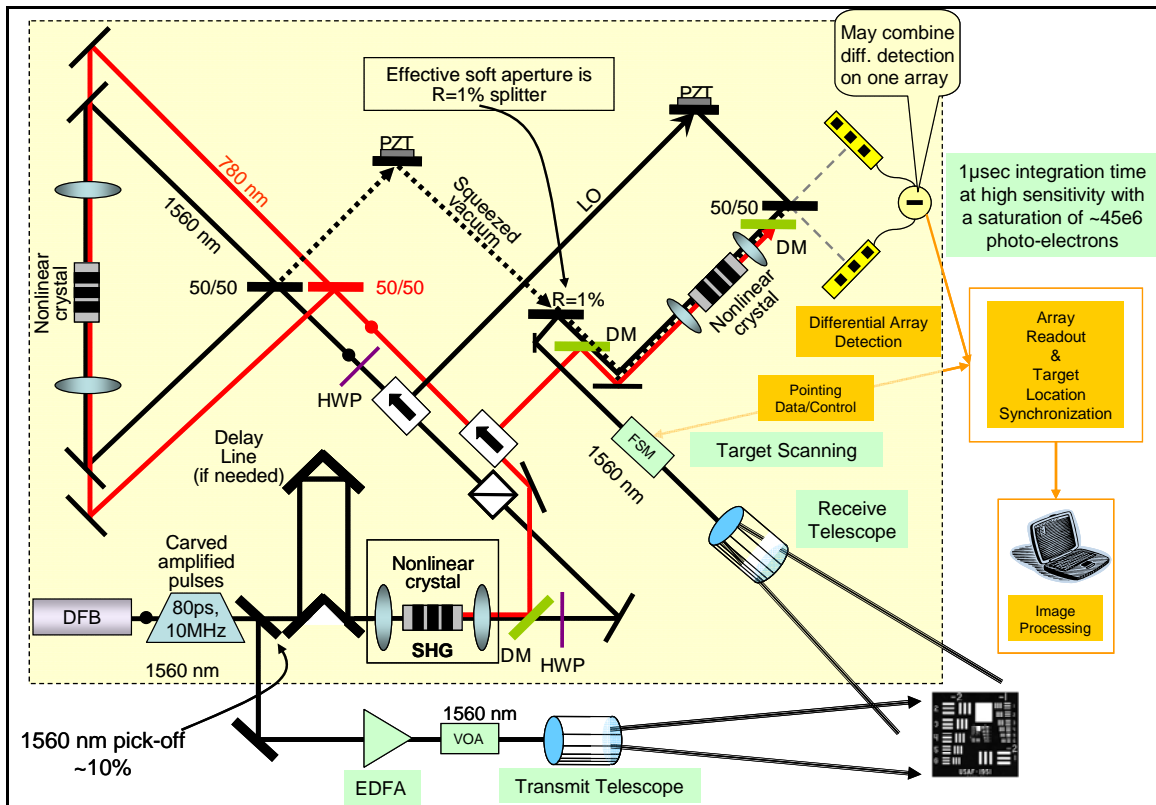

Figure 40: Design layout of QSP LADAR

The scattered light from the target is collected by a receive telescope and directed by a scanning mirror onto a linear detector array operated as a balanced mixer. Operation of the detector as a balanced mixer is essential for observing the squeezing phenomenon in which the noise (in one quadrature component) is below the standard quantum noise level of a coherent state. The detected signal is then sent to a computer for image processing. Both a direct image and the modulation transfer function (MTF) of the image can be collected during LADAR system operation, although only direct image generation is shown in Figure 40. The use of MTF analysis should show quantitatively the spatial frequency enhancement realized by employing QIE in the LADAR receiver. Images, such as those depicted in Figure 10, can be created with a baseline LADAR and with the baseline LADAR enhanced with the PSA activated separately, the SVI activated separately and both PSA and SIV activated together. The resultant images from a quantum LADAR can be contrasted with those collected from the baseline LADAR with both PSA and SVI inactive.

Theory and proof-of-concept experiments predict that quantum enhancement should enable a standoff LADAR to function with remarkably improved resolution. However, future development of such a complex LADAR comes with concomitant risk. Significant risks associated with this LADAR development are summarized in this section ranked in order of our estimate of severity.

1) **Preservation of squeezing throughout the LADAR System:** Although for the table top demonstration proposed in this program the location of the soft aperture is well defined, in a practical system the location of the aperture is more complex. Therefore, the location for injection of the squeezed vacuum signal may be problematic. Moreover, preserving the integrity of the squeezing throughout the entire imaging system is a complex undertaking. A high level of squeezing must be retained through i) a half wave plate, ii) a polarization beam splitter, iii) reflection from a partially-reflecting mirror (or some more complicated soft-aperture object), iv) the PSA system, and v) the homodyne mixing system. Throughout this entire optical path there are numerous opportunities for amplitude and coherence loss in the signal.

2) **Homodyne Detection of SVI:** Homodyne detection of a squeezed-vacuum injected signal across a large linear or 2-D array poses a significant risk. The homodyne detection system must be carefully matched to the quadrature that is squeezed. Even if this is achieved for a single spatial mode, maintenance of this matching across the entire array will require an extremely precise imaging system.

3) **Mode Matching of PSA and SVI:** Matching the amplified modes of the PSA to the squeezed modes of the SVI must be achieved so that the amplified quadrature of the PSA has a maximum mode match with the squeezed quadrature of the SVI.

4) PSA Pump Power: Limited PSA pump power could significantly restrict LADAR operation. In the direct-detection experiments reported in Section 3.0, a shot-noise-limited regime was determined to be around 10^6 photons per pixel; however, all resolution measurements were undertaken in the dark-noise-limited regime. It is not clear at this time in which regime the LADAR will be operated to satisfy several important criteria—low dark noise, quantum efficiency that is reasonable with respect to the amount of PSA gain attained, and sufficiently strong amplified signals. Although the attainment of a suitable pump light source remains a significant risk, this is a technical problem rather than a scientific problem. The peak pump-source power needs to be greater than 10 kW for generating sufficient image gain. Moreover, the pump must provide stable, high repetition rate pulses that have a flat-top temporal profile with short rise and fall times to avoid any temporal averaging and to minimize mode-matching effects for PSA and SVI. Low-frequency pump noise must also be minimized, as it will adversely affect the local oscillator.

5) Imaging Detector: Multipixel homodyne imaging detection is a risk, although the risk is technical and not scientific. For our imaging detector, measurements will have to be made at baseband where numerous noise sources must be overcome. As we have encountered in QSP Phase I, detector companies that package the detectors with an electronic backplane provide limited information from which to optimize measurements. The risk to the program is allowing too much effort to be devoted to detector engineering rather than to PSA and SVI LADAR characterization.

6) Relative Signal Phase Stabilization: As a technical rather than a scientific risk, several servo loops will need to be implemented to stabilize the relative phases between the pump and signal. Also, optical paths within the PSA and SVI sections must be maintained identical in length, and optical elements within those paths must be selected to minimize mismatch between the pump and signal beams.

These risks enumerated above pertain to the SVI and PSA functions of the LADAR and present significant challenges that do not require scientific breakthroughs as much as herculean technological efforts.

6.0   SUMMARY

In summary, the resolution of a homodyne LADAR can be enhanced significantly by applying quantum optical techniques in the receiver. This study explored theoretically three quantum sensor types, and developed two laboratory proof-of-concept demonstrations for angle-angle resolution improvement and for range resolution improvement. With a quantum image enhancer (QIE) inserted between the receive optics and the detector of a classical homodyne LADAR, an angular cell resolution improvement of 10x can be realized. The QIE is comprised of two key elements—a squeezed-vacuum injector (SVI) that restores the high spatial frequencies lost by attenuation in soft-aperture entrance optics in the LADAR and a phase sensitive amplifier (PSA) that overcomes the inefficiency of the homodyne detector. When the QIE is combined with a phase-conjugate optical coherence tomographic (PC-OCT) technique for a two-fold range resolution enhancement, a 200-fold voxel (angle-angle-range) improvement is possible for a standoff homodyne LADAR. Underlying theory was established that relates the LADAR's signal-to-noise ratio (SNR) to its angular resolution. This modeling provided the framework within which various detection scenarios could be compared when resolving specular returns and fully-developed speckle scatter from a LADAR target. The efficacy of using non-classical light (a Type-1 sensor) for propagation to a target was shown to offer, at most, an inconsequential target-detection advantage for the highly-lossy scenarios associated with LADAR operation over 1-100 km standoff ranges. Several key no-go theorems were developed with respect to both Type-1 and Type-3 sensors. Two alternative quantum sensor categories—Type-2 using classical light with a non-standard receiver and Type-3 using transmitter-receiver entanglement—were studied theoretically. The approach employing a QIE for a Type-2 sensor was shown to present the most promise. The characteristics of the three types of sensors and a summary of salient theoretical results related to each type were presented. In addition, extensive modeling based on the developed theory showed Type-2 sensor image improvement realized by employing SVI, PSA and combined SVI and PSA. Experimental results validating the QIE concept were shown using a PSA for angle image improvement and PC-OCT for two-fold range improvement, as well as for dispersion compensation. A Type-3 sensor technique, known as quantum illumination, was also studied theoretically and its application to secure communication briefly summarized. Ghost imaging applied to standoff sensing was examined and its underlying theory comprehensively explored. Finally, a conceptual design was introduced for a homodyne LADAR Type-2 sensor incorporating both PSA and SVI in a quantum-enhanced receiver.

7.0   REFERENCES

[1] B. I. Erkmen and J. H. Shapiro, "Phase-conjugate optical coherence tomography," Phys. Rev. A **74**, 041601(R) (2006).

[2] B. I. Erkmen and J. H. Shapiro, "Unified theory of ghost imaging with Gaussian-state light," Phys. Rev. A **77**, 043809 (2008).

[3] R. Nair and H. P. Yuen, "No-go theorem for Type-1 noiseless binary detection," Harris team internal memorandum, Feb. 11, 2008.

[4] R. Nair and H. P. Yuen, "Lower bound on error probability of Type III noiseless binary detection with signal number diagonal states," Harris team internal memorandum, May 7, 2009.

[5] H. P. Yuen and R. Nair, "Classicalization of nonclassical quantum states in loss and noise — some no-go theorems," arXiv:0905.0855 [quant-ph].

[6] J. H. Shapiro, "Error bounds for conventional soft-aperture coherent-detection imaging," Harris team internal memorandum, Dec. 21, 2007.

[7] J. H. Shapiro, "Error bounds for soft-aperture coherent-detection imaging with squeezed-vacuum injection," Harris team internal memorandum, Feb. 26, 2008.

[8] J. H. Shapiro, "Error bounds for soft-aperture homodyne-detection imaging with squeezed-vacuum injection and phase-sensitive amplification," Harris team internal memorandum, Oct. 4, 2008.

[9] Z. Dutton, "Scaling of LIDAR target resolution: speckle case," Harris team internal memorandum, Feb. 8, 2008.

[10] Z. Dutton, "Resolution improvement with squeezed vacuum injection," Harris team internal memorandum, June 18, 2008.

[11] J. H. Shapiro, "Optics configuration for squeezed-vacuum injection," Harris team internal memorandum, June 17, 2008.

[12] J. H. Shapiro, "Modulation transfer function analysis for squeezed-vacuum injection," Harris team internal memorandum, August 4, 2008.

[13] S. Guha, "The SVI + PSA receiver: propagation model, an MTF analysis, image simulations, and results," Harris team internal slide set, Jan. 29, 2009.

[14] S. Lloyd, "Enhanced sensitivity of photodetection via quantum illumination," Science **321**, 1463 (2008).

[15] S.-H. Tan, B. I. Erkmen, V. Giovannetti, S. Guha, S. Lloyd, L. Maccone, S. Pirandola, and J. H. Shapiro, "Quantum illumination with Gaussian states," Phys. Rev. Lett. **101**, 253601 (2008).

[16] S. Guha, "Receiver design to harness quantum illumination advantage," arXiv:0902.2932 [quant-ph], to be presented at the 2009 International Symposium on Information Theory, Seoul Korea.

[17] J. H. Shapiro, "Quantum illumination for the one-versus-two target scenario," Harris team internal memorandum, Aug. 4, 2008, typos corrected Aug. 12, 2008.

[18] J. H. Shapiro, "Secure communication with Gaussian-state quantum illumination," arXiv:0903.3150 [quant-ph].

[19] J. H. Shapiro, "Defeating passive eavesdropping with quantum illumination," arXiv:0904.2490.

[20] R. Meyers, K. S. Deacon, and Y. Shih, "Ghost-imaging experiment by measuring reflected photon," Phys. Rev. A **77**, 041801(R) (2008).

[21] Y. Shih, "The physics of ghost imaging," arXiv:0805.1166 [quant-ph].

[22] B. I. Erkmen and J. H. Shapiro, "Signal-to-noise ratio of Gaussian-state ghost imaging," Phys. Rev. A **79**, 023833 (2009).

[23] J. H. Shapiro, "Computational ghost imaging," Phys. Rev. A **78**, 061802(R) (2008).

[24] Y. Bromberg, O. Katz, and Y. Silberberg, "Ghost imaging with a single detector," arXiv:0812.2633 [quant-ph].

[25] J. H. Shapiro, B. A. Capron, and R. C. Harney, "Imaging and target detection with a heterodyne-reception optical radar," Appl. Opt. **20**, 3292 (1981).

[26] H. P. Yuen, "Reduction of quantum fluctuation and suppression of the Gordon-Haus effect with phase-sensitive linear amplifiers," Opt. Lett. **17**,73 (1992).

[27] S. K. Choi, M. Vasilyev, and P. Kumar, "Noiseless optical amplification of images," Phys, Rev, Lett. **83,** 1938(1999); erratum: **84**, 1361 (2000).

[28] O.-K. Lim, G. Alon and P. Kumar, "Generation and measurements of high extinction-ratio optical pulses." Harris team internal memorandum, Nov. 11, 2008.

[29] O.-K. Lim, G. Alon and P. Kumar, "Resolution enhancement in imaging with a phase-sensitive amplifier (PSA)." Harris team internal memorandum, Dec.2, 2008.

[30] N. Stelmakh and M. Vasilyev, "Classical amplification and de-amplification with inhomogeneous pump," Harris team internal memorandum, Oct. 9, 2008.

[31] Z. Dutton, "Scaling of LIDAR target resolution: specular case," Harris team internal memorandum, Jan. 24, 2008, revised Feb. 8, 2008.

[32] J. H. Shapiro, "Error bounds for conventional shot-noise limited imaging", Harris team internal memorandum, Nov. 8, 2007.

[33] M. Vasilyev, "On the quantum theory of optical parametric amplifier with inhomogeneous pump," Harris team internal memorandum, Oct. 9, 2008.

[34] M. Vasilyev, "On the spatial bandwidth estimate for plane-wave-pump OPA," Harris team internal memorandum, Oct. 9, 2008.

[35] M. Vasilyev, N. Stelmakh, and P. Kumar, "Estimation of the spatial bandwidth of an optical parametric amplifier with plane-wave-pump," submitted to J. Mod. Optics.

[36] M. Vasilyev, N. Stelmakh, and P. Kumar, "Parametric gain for multimode light," *the 39th Winter Colloquium on the Physics of Quantum Electronics (PQE-2009)*, Snowbird, Utah, January 4–8, 2009.

[37] M. Vasilyev, N. Stelmakh, and P. Kumar, "Investigation of phase-sensitive image amplification with elliptical Gaussian pump," to be presented at the *Conference on Lasers and Electro-Optics 2009*, Baltimore, MD, May 31–June 5, 2009, paper JWA6.

[38] M. Vasilyev, N. Stelmakh, and P. Kumar, "Phase-sensitive image amplification with elliptical Gaussian pump," submitted to Opt. Express.

[39] A. F. Abouraddy, M. B. Nasr, B. E. A. Saleh, A. V. Sergienko, and M. C. Teich, "Quantum-optical coherence tomography with dispersion cancellation," Phys. Rev. A **65**, 053817 (2002).

[40] M. B. Nasr, B. E. A. Saleh, A. V. Sergienko, and M. C. Teich, "Demonstration of dispersion-canceled quantum-optical coherence tomography," Phys. Rev. Lett. **91**, 083601 (2003).

[41] J. Le Gouët, D. Venkatraman, and F. N. C. Wong, "Optical parametric amplifier performance for PC-OCT," Harris team internal memorandum, Oct. 9, 2008.

[42] J. Le Gouët, D. Venkatraman, and F. N. C. Wong, "Single-pass baseline measurements for phase-conjugate optical coherence tomography," Harris team internal memorandum, Dec. 10, 2008.

8.0 ACRONYM LIST

BPSK	Binary Phase Shift Keyed
CCD	Charge Coupled Device
CS	Coherent State
CWDM	Course Wavelength Division Multiplexing
EDFA	Erbium-Doped Fiber Amplifier
FFT	Fast Fourier Transform
BPM	Beam Propagation Model
FWHM	Full Width Half Maximum
iid	independent identically distributed
KTP	Potassium-Titanyl-Phosphate
LADAR	LAser Detection And Ranging
LPD	Low Probability of Detection
LPI	Low Probability of Intercept
MTF	Modulation Transfer Function
OCT	Optical Coherence Tomography
OPA	Optical Parametric Amplifier
PCR	Phase-Conjugate Ranging
PC-OCT	Phase-Conjugate Optical Coherence Tomography
PIA	Phase Insensitive Amplifier
PPKTP	Periodically-Poled Potassium-Titanyl-Phosphate
PP-MgO:LN	Periodically Poled Magnesium Oxide-doped Lithium Niobate
PSA	Phase-Sensitive Amplifier
QI	Quantum Illumination
QIE	Quantum Image Enhancer
QKD	Quantum Key Distribution
Q-OCT	Quantum Optical Coherence Tomography
QSP	Quantum Sensors Program
SHG	Second Harmonic Generator
SLM	Spatial Light Modulator
SMF	Single Mode Fiber (SMF28 is a Corning single mode fiber)
SND	Signal-Number Diagonal
SNR	Signal-to-Noise Ratio
SPDC	Spontaneous Parametric Down Conversion
SVI	Squeezed Vacuum Injection